

NASA Technical Memorandum 87756

Buckling Characteristics of Hypersonic Aircraft Wing Tubular Panels

William L. Ko

*Ames Research Center
Dryden Flight Research Facility
Edwards, California*

John L. Shideler

*Langley Research Center
Hampton, Virginia*

Roger A. Fields

*Ames Research Center
Dryden Flight Research Facility
Edwards, California*



National Aeronautics
and Space Administration

**Scientific and Technical
Information Branch**

1986

Introduction

When the speed of an aircraft reaches the hypersonic range, aerodynamic heating becomes severe. Some of the hypersonic flight vehicle structural concepts that have been advanced use a thermal protection system (TPS) to prevent the structure from overheating. For example, the Space Shuttle uses a TPS designed to limit the structural temperature to 350°F (a warm structure). A different concept proposed for future hypersonic aircraft (ref. 1) was an aerodynamically acceptable wavy heat shield made of heat resistant metal, such as René 41, to limit the structural temperature to about 1350°F (a hot structure). Compression buckling is a major concern for hot structures because of the combined effects of aerodynamic load, thermal stress, and reduction in material moduli (i.e., modulus of elasticity E and shear modulus G).

Studies of structures for future hypersonic flight vehicles have identified advanced structural concepts which show promise of having low structural unit mass and high buckling strength (refs. 2 to 13). Since curved shell sections exhibit high local buckling strength, most of the structural panel concepts investigated used curved surfaces to achieve high buckling strength. Two of the hot structural panel concepts investigated were beaded panels and circular tubular panels (ref. 1). Results from extensive buckling studies of René 41 beaded panels and aluminum circular tubular panels are reported in reference 9 and references 2 to 6, respectively. All the test results for tubular panels were obtained from single-panel, room-temperature loading tests under laboratory conditions. Furthermore, only limited buckling data have been reported on René 41 non-circular tubular panels, which (based on the analysis methods of reference 6) are more efficient than circular tubular panels for lightly loaded conditions.

Thus, to characterize the buckling behavior of the tubular panels under combined loads and at elevated temperatures, five René 41 noncircular tubular panels (fig. 1) were attached to the wing root region of the hypersonic wing test structure (HWTS, described in the *Test Equipment* section). These five panels, which replaced beaded wing panels on the HWTS (refs. 9, 12, and 13), were exposed to extensive nondestructive buckling tests under different combined load conditions (axial compression, bending under lateral pressure, and shear) at uniform temperatures of 70°F, 550°F, and 1000°F. The use of uniform elevated test temperatures caused a reduction in material moduli (E and G) and minimized thermal stresses due to temperature gradients. Although they are difficult to calculate and measure,

thermal stresses will undoubtedly have to be considered in the future if hot structures are to be used. The buckling loads were estimated through use of the force/stiffness (F/S) method of plotting the test data (ref. 11), and the results were compared with theoretically predicted buckling interaction curves.

Symbols

C_j	coefficients ($j = 1, 2, \dots, 6$)
D	generalized strain variable
D_{cr}	generalized strain variable at buckling
E	modulus of elasticity, psi
E_{sec}	secant modulus, psi
E_{tan}	tangent modulus, psi
F	applied load, lbf
F_{cr}	buckling load, lbf
F^*	maximum applied load, lbf
F_{703}	applied load at HWTS location 703, lbf
$(F_{703})_{cr}$	value of F_{703} at predicted buckling point, $k F_{703}^*$, lbf
F_{703}^*	maximum value of F_{703} in nondestructive buckling test, lbf
f_b, f_c, f_s	bending, compression, and shear stresses, psi
f_{cb}, f_{cc}, f_{cs}	bending, compression, and shear local buckling stresses of circular elements, psi
f_{cr}	stress intensity at buckling, psi
f_{cy}	compression yield stress, psi
f_{pl}	proportional limit stress (threshold of inelastic stress region), psi
G	shear modulus, psi
i	index, 1 to 3
K_s	$= 4 \left(\frac{S_c^2}{RT} \sqrt{1 - \nu^2} \right)^{0.514}$
k	extrapolation factor, F_{cr}/F^*
L	panel length
m	exponent in expression of D
N_x	panel axial compression stress resultant, lbf/in.
$(N_x)_{cr}$	value of N_x at buckling, $k N_x$, lbf/in.
N_x^*	value of N_x at maximum applied load F^*

N_{xy}	panel shear stress resultant, lbf/in.
$(N_{xy})_{cr}$	value of N_{xy} at buckling, $k N_{xy}$, lbf/in.
N_{xy}^*	value of N_{xy} at maximum applied load F^*
n	shape factor in Ramberg-Osgood stress-strain approximation
p	lateral pressure, psi
R	radius of circular arc of panel tube cross section
R_b, R_c, R_s	ratios of actual stress to critical stress for bending, compression, and shear
RSG	output of rosette strain gage
RSG*	output of rosette strain gage at maximum applied load F^*
$\overline{\text{RSG}}$	output of rosette strain gage with structure at uniform elevated temperatures without applied mechanical load
S_c	arc length of circular arc element of panel tube cross section, $2\alpha R$
SG	output of axial strain gage
$\overline{\text{SG}}$	output of axial strain gage with structure at uniform elevated temperatures without applied mechanical load
T	temperature, °F
t	thickness of tubular wall, in.
\bar{t}	equivalent extensional thickness, in.
w	unit panel weight, lbm/in ²
α	half-angle of circular arc of panel tube, $\frac{S_c}{2R}$
γ	shear strain
γ_{cr}	shear strain at buckling
ϵ_b	bending strain
$(\epsilon_b)_{cr}$	bending strain at buckling
ϵ_c	axial compression strain
$(\epsilon_c)_{cr}$	axial compression strain at buckling
η_i	plasticity correction factor ($i = 1$ to 3)
η_{tan}	plasticity correction factor calculated from tangent modulus
η_{sec}	plasticity correction factor calculated from secant modulus

η_1	$= \eta_{tan}$
η_2	$= \eta_{sec}$
η_3	$= (\eta_1 \eta_2)^{1/2}$
ν	Poisson's ratio

Panels

Five identical René 41 tubular panels were designed and fabricated to replace the root-chord wing panels of the HWTS. The design of the panels, described in references 2 and 6, used a random search optimization routine to determine values of the cross-section variables which constitute a minimum mass per unit area subject to specified applied load, geometric, and failure constraints. The panel design loads were $N_x = 800$ lbf/in., $N_{xy} = 250$ lbf/in., and $p = 0.75$ psi at $T = 1350^\circ\text{F}$. The resulting design, which was constrained by a minimum skin thickness of 0.016 in., is shown in figure 1. Although the average thickness of each chemically milled sheet was determined to be 0.0168 in., the design thickness of 0.016 in. was used in the analyses throughout this paper.

Each tubular panel was made of two formed René 41 alloy sheets seam welded together to form five flat regions (double sheets) and four noncircular tubular regions (i.e., flattened tubes). The René 41 was procured in a solution annealed (1975°F) condition. Prior to welding, the circular arcs in each sheet were incrementally brake formed, and the end closures were die formed. Doublers were spot welded to both sides at each end of the panel to prevent local end failure and to reduce excessive deformations due to shear loads. After the final weld assembly, the panels were aged for 1 hour at 1650°F followed by 10 hours at 1400°F . Figure 2 shows a photograph of one of the fabricated tubular panels. The panel had eight attachment points for z-shaped clips to support the heat shields, which are described subsequently. A detailed description of the panel fabrication process is given in references 3 and 6.

Analysis

Local instability is, by design, the critical failure mode for the tubular panel shown in figure 1. Although local and general instability are nearly equal under some combined load conditions (ref. 2), it is likely that local instability would occur at the same time, even if general instability were to occur first. Consequently, this paper primarily addresses local buckling behavior and the equations governing local buckling. (The general buckling equations used in the design and analysis of the tubular panel are

those identified by Euler (wide column) for compression and by Timoshenko for shear. The equations, which include the effects of plasticity and bending due to an initial imperfection, are given in refs. 2 and 6.)

Local Buckling

For a tubular panel with tubes of completely circular cross sections, the equations for local buckling (bead crippling) of circular arc elements of the panel in compression, bending, and shear may be written in the current notation as follows:

Compression (eq. (14-3) of ref. 2):

$$f_{cc} = 0.738\eta_3 E \left(\frac{t}{R} \right)^{1.19} \quad (1)$$

Bending (eq. (12-33) of ref. 2):

$$f_{cb} = 0.77\eta_3 E \left(\frac{t}{R} \right)^{1.15} \quad (2)$$

Shear (eq. (12-34) of ref. 2):

$$f_{cs} = \eta_2 G K_s \left(\frac{t}{S_c} \right)^2 \quad (3)$$

where

$$K_s = 4 \left(\frac{S_c^2}{Rt} \sqrt{1 - \nu^2} \right)^{0.514} \quad (4)$$

Buckling equations (1) and (2) are valid for the range $20 < \frac{R}{t} < 120$, and equation (3) is valid for

$$\frac{S_c^2}{Rt} \sqrt{1 - \nu^2} > 50$$

To apply equation (1) to the noncircular tubular panel, a knockdown factor of 0.86 is recommended. (See ref. 6, p. 46.) Equations (2) and (3) are applied directly to the flattened tubular panel without modification. The buckling equation for compression of the noncircular tubular panel is then

$$f_{cc} = (0.86)(0.738)\eta_3 E \left(\frac{t}{R} \right)^{1.19}$$

or

$$f_{cc} = 0.635\eta_3 E \left(\frac{t}{R} \right)^{1.19} \quad (5)$$

Equations (5), (2), and (3) are used to calculate the theoretical buckling strains $f_{cc}/\eta_3 E$, $f_{cb}/\eta_3 E$, and

$f_{cs}/\eta_2 G$ in compression, bending, and shear, respectively, for use in the force/stiffness plots of the non-destructive buckling data described in a subsequent section.

Compression-Shear Interaction

The standard interaction equation for buckling failure of a panel under combined loads of axial compression and shear is (ref. 2)

$$R_c + R_s^2 = 1$$

where R_c and R_s are ratios of the actual compression and shear stresses in the panel at failure under combined loads to the critical stresses in pure axial compression and in pure shear, respectively. This equation is used for all buckling failure modes. For general instability, the stress ratios are defined as

$$R_c = \frac{N_x}{(N_x)_{cr}}$$

$$R_s = \frac{N_{xy}}{(N_{xy})_{cr}}$$

For the local buckling mode for the noncircular tubular panel (bead crippling), the stress ratios are defined as

$$R_c = \frac{f_c}{f_{cc}} + \frac{f_b}{f_{cb}}$$

$$R_s = \frac{f_s}{f_{cs}}$$

The stress ratio for local buckling in compression accounts for coupling between compression and bending. This coupling occurs even when zero lateral pressure is applied to the panel because an assumed initial imperfection of $0.001L$ provides a moment arm by which compression can always produce a bending stress. (See ref. 2.)

Plasticity

The plasticity correction factors which appear in the local buckling equations are defined as (ref. 2, p. 31)

$$\eta_1 = \eta_{tan} = E_{tan}/E \quad (6)$$

$$\eta_2 = \eta_{sec} = E_{sec}/E \quad (7)$$

$$\eta_3 = (\eta_1 \eta_2)^{1/2} = (\eta_{tan} \eta_{sec})^{1/2} \quad (8)$$

Through use of a modified Ramberg-Osgood stress-strain approximation (see ref. 2), the tangent and secant moduli at the buckling stress are

$$E_{tan} = \frac{f_{cr}}{(f_{cr}/E) + n[0.002(f_{cr}/f_{cy})^n - 0.00001]} \quad (9)$$

and

$$E_{\text{sec}} = \frac{f_{\text{cr}}}{(f_{\text{cr}}/E) + 0.002(f_{\text{cr}}/f_{\text{cy}})^n - 0.00001} \quad (10)$$

where

$$f_{\text{cr}} > f_{\text{pl}} = f_{\text{cy}}(0.005)^{\frac{1}{n}} \quad (11)$$

and

$$E_{\text{tan}} = E_{\text{sec}} = E \quad \text{if} \quad f_{\text{cr}} < f_{\text{pl}}$$

The shape factor n in the Ramberg-Osgood stress-strain approximations for René 41 (eqs. (9), (10), and (11)) is taken as $n = 25.0$ at 70°F , 22.2 at 550°F , and 18.5 at 1000°F . Figures 3, 4, and 5 show the plots of equivalent elastic stress f_{cr}/η_i ($i = 1, 2, 3$) as a function of actual stress f_{cr} for the three respective temperatures 70°F , 550°F , and 1000°F . Values of the modulus of elasticity E and the shear modulus G for René 41 are shown in figure 6 as a function of temperature (ref. 14). With the aid of figures 3 to 6, the theoretical buckling strains in compression $(\epsilon_c)_{\text{cr}}$, in bending $(\epsilon_b)_{\text{cr}}$, and in shear γ_{cr} can be calculated from equations (5), (2), and (3) as

$$(\epsilon_c)_{\text{cr}} = \frac{f_{\text{cc}}}{\eta_3 E} \quad (12)$$

$$(\epsilon_b)_{\text{cr}} = \frac{f_{\text{cb}}}{\eta_3 E} \quad (13)$$

$$\gamma_{\text{cr}} = \frac{f_{\text{cs}}}{\eta_2 G} \quad (14)$$

The values of $(\epsilon_c)_{\text{cr}}$, $(\epsilon_b)_{\text{cr}}$, γ_{cr} , η_2 , η_3 , E , G , and f_{cy} for the different temperatures are given in table 1.

Force/Stiffness Method

The purpose of conducting nondestructive buckling tests instead of destructive buckling tests was to avoid the cost associated with destructive tests of a large number of panels. In destructive buckling tests, only one buckling data point for one load condition can be generated from each test panel. However, through use of the F/S method to predict the buckling strength, a wide range of buckling data can be generated from each test panel for different loading and temperature conditions. The F/S method was advanced by Jones and Greene (ref. 11) for the prediction of general and local buckling strengths of structural components whose buckling behavior is complex or nonlinear.

Since local buckling is, by design, the failure mode for the tubular panels, the F/S method used in this paper is one developed to predict local buckling failure. The method uses a plot of F against F/D ,

where F is the applied load and D is a generalized strain variable which accounts for axial compression, bending, and shear components. The generalized strain variable D is given by

$$D = \frac{\epsilon_c}{(\epsilon_c)_{\text{cr}}} + \frac{\epsilon_b}{(\epsilon_b)_{\text{cr}}} + \left(\frac{\gamma}{\gamma_{\text{cr}}}\right)^m \quad (15)$$

and the predicted local buckling occurs when

$$D = D_{\text{cr}} = 1 \quad \text{and} \quad \frac{F}{D} = \frac{F_{\text{cr}}}{D_{\text{cr}}} = F_{\text{cr}} \quad (16)$$

The strains ϵ_c , ϵ_b , and γ are measured with strain gages, and the buckling strains $(\epsilon_c)_{\text{cr}}$, $(\epsilon_b)_{\text{cr}}$, and γ_{cr} are calculated from equations (12), (13), and (14), respectively. (See table 1.) The exponent m in equation (15) was empirically determined to be 2 for most types of panels including the completely circular tubular panels (ref. 5). For the present F/S analysis, $m = 2$.

Equations (15) and (16) represent a buckling strain interaction surface which is the basis for the limit strain lines used in the F/S plots. Figure 7 shows a graphical illustration of the F/S method, which requires extrapolation of the curve fitting the test data points. The buckling failure load is determined from the intersection of the extrapolated curve and the limit strain line. The accuracy of buckling-failure-load prediction with the F/S method depends on (1) the location of strain gages so that they measure strain which is sensitive to the impending buckling mode shape, (2) the distance of extrapolation (that is, how close the final test data point is to the limit strain line), (3) the accuracy of the curve fitting, and (4) the accuracy with which the limit strain line itself is determined (e.g., if the critical strains are determined experimentally for a specific configuration, they may be more accurate than if they are determined analytically from general equations).

The extrapolation of the F/S test data points to the intersection with the limit strain line was accomplished through least-squares fitting of the test data through use of the following equation from reference 11:

$$\frac{F}{D} = \frac{1 + C_1 F + C_2 F^2}{C_3 + C_4 F + C_5 F^2 + C_6 F^3} \quad (17)$$

The buckling value of F (the intersection point F_{cr}) was determined by setting $D = 1$ in equation (17). In the present F/S analysis, D was expressed as follows:

Room temperature:

$$D = \frac{SG_1 + SG_2}{2(\epsilon_c)_{cr}} + \frac{|SG_1 - SG_2|}{2(\epsilon_b)_{cr}} + \left(\frac{2|RSG_2 - RSG_3|}{\sqrt{3}\gamma_{cr}} \right)^2 \quad (18)$$

Elevated temperatures:

$$D = \frac{(SG_1 - \overline{SG}_1) + (SG_2 - \overline{SG}_2)}{2(\epsilon_c)_{cr}} + \frac{|(SG_1 - \overline{SG}_1) - (SG_2 - \overline{SG}_2)|}{2(\epsilon_b)_{cr}} + \left[\frac{2|(RSG_2 - \overline{RSG}_2) - (RSG_3 - \overline{RSG}_3)|}{\sqrt{3}\gamma_{cr}} \right]^2 \quad (19)$$

where SG_1 and SG_2 are the outputs of the axial strain gages placed respectively on the lower and upper outermost fibers of the tube at the panel center region, and RSG_2 and RSG_3 are the outputs of delta-rosette strain gage legs other than the leg parallel to the tubes. The bar indicates the initial nonzero strain gage readings at elevated temperatures when no mechanical loads were applied (panels were soaked at uniform temperature to determine these initial strains due to gage drift, apparent strain, and unintentional temperature nonuniformity).

Panel Buckling Loads

After the buckling load F_{cr} is determined using the F/S method, the associated panel axial compression stress resultant at buckling $(N_x)_{cr}$ and panel shear stress resultant at buckling $(N_{xy})_{cr}$ must be determined. If N_x^* and N_{xy}^* are respectively the panel axial compression and shear stress resultants associated with the maximum applied load F^* (see fig. 7), and if $(RSG_1^* - \overline{RSG}_1)$, $(RSG_2^* - \overline{RSG}_2)$, and $(RSG_3^* - \overline{RSG}_3)$ are the readings of the three legs of the rosette strain gage when $F = F^*$ ($(RSG_1^* - \overline{RSG}_1)$ being in the axial direction), then N_x^* and N_{xy}^* can be calculated as

$$N_x^* = E\bar{t}(RSG_1^* - \overline{RSG}_1) \quad (20)$$

$$N_{xy}^* = \frac{4}{\sqrt{3}}Gt|(RSG_2^* - \overline{RSG}_2) - (RSG_3^* - \overline{RSG}_3)| \quad (21)$$

where $\bar{t} = 0.0368$ in. is the equivalent extensional thickness of the panel, $t = 0.016$ in. is the thickness of the tubular wall, and RSG_i ($i = 1$ to 3) are the rosette strain gage readings at $F = F^*$.

If the extrapolation factor k (see fig. 7) is defined as

$$k \equiv \frac{F_{cr}}{F^*} \quad (22)$$

then $(N_x)_{cr}$ and $(N_{xy})_{cr}$ can be estimated from

$$(N_x)_{cr} = k N_x^* \quad (23)$$

and

$$(N_{xy})_{cr} = k N_{xy}^* \quad (24)$$

The values of $(N_x)_{cr}$ and $(N_{xy})_{cr}$ thus obtained from test data are used in constructing the buckling interaction figures.

Test Equipment

Combined Loads

Hypersonic wing test structure. The hypersonic wing test structure (HWTS), shown in figure 8, has a planform area of 85 ft² and is a portion of a proposed hypersonic research airplane (HRA) wing shown in figure 9. The HWTS was constructed based on the knowledge gained from the study of hot structural concepts for a Mach 8 hypersonic cruise vehicle with a 2.5g pull-up capability (refs. 1 and 12). The HWTS was tested extensively in the past (ref. 13) to evaluate the hot-wing structural concept and to evaluate flight loads instrumentation, high-temperature calibration methods, and temperature simulation techniques. The beaded skin panels and corrugated spars and ribs are made of René 41, a nickel-base alloy. The heat shields are single-sheet panels which are slightly corrugated in the chordwise direction and are made of René 41 alloy except for those along the leading edge, which are made of TD Ni-20Cr. The René 41 heat shields are designed for locations where the surface temperature is less than 1800°F, and those made of TD Ni-20Cr are capable of operating with surface temperatures in excess of 1800°F. The heat shields are separated from the beaded skin panel by z-shaped support clips in order to minimize heat conduction from the heat shields to the substructure. The HWTS is connected to the support structure through a transition section and is mounted inverted so that wing loads produce compression on the lower surface of the HWTS. The transition section provides a load distribution buffer between the support structure and the test portion of the wing. The upper wing root zone (lower surface of HWTS) is the most highly compression-loaded area, and the five beaded panels there were replaced with five tubular panels for the nondestructive buckling tests. Figure 10 shows the HWTS with the heat shields removed to reveal the substructure and the z-shaped clips for supporting the heat shields.

Mechanical loading system. Figure 11 shows the location of the applied load points on the HWTS and

the locations of the five test tubular panels. Twenty closed-loop channels were used to control electrohydraulic equipment which applied mechanical loads to the test structure at the load points. Ten hydraulic jacks were used to apply vertical loads (simulation of lift load) to the HWTS to induce compression loads in the test panels. Eight of those jacks applied loads through two-point whiffletrees. Horizontal loads (simulation of drag and thermal loads from adjacent vehicle structure) were applied with the remaining 10 hydraulic jacks at single load points at the fore and aft edges of the HWTS to induce shear loads in the test panels. Pressure loads (which induced bending loads in the panels) were applied normal to the upper surface of each test panel by using a 0.003-in.-thick stainless-steel pressure pan positioned over each test panel. Each pan, which was bolted to the perimeter of a panel, thus formed one side of a pressure box. (See fig. 12.)

Heating system. The system used to simulate aerodynamic heating of the HWTS is shown in figure 13. The system was designed to heat the entire upper and lower surfaces of the HWTS to the temperatures corresponding to a Mach 8 flight profile. Infrared quartz lamps mounted on water-cooled polished aluminum reflectors (as shown in fig. 14) were used to provide radiant heat. The system consisted of separate lower and upper heating units which were slightly contoured to match the surface shape of the HWTS. The units were mounted on rollers and tracks (see fig. 13) so that they could be easily removed for access to the HWTS and then be precisely repositioned. The heating units were positioned with the reflector surfaces approximately 6 in. from the heat shields of the HWTS. Gaps in the lower heater were provided along the spar caps to allow clearance for connectors from the vertical loading system (see fig. 13). To fill in those gaps between load points, a double row of quartz lamps mounted on separate long, narrow water-cooled aluminum reflectors (i.e., strip heaters) was installed parallel to the spar caps. The temperatures of the panels were controlled by signals to the heating system from feedback thermocouples attached to the heat shield exterior surfaces. The plumbing for the reflector cooling water included a pressure gage for each feed line to assure adequate coolant pressure. During the elevated-temperature tests, insulation curtains were draped around the HWTS and the heating system to reduce radiative and convective heat losses. (See fig. 13.)

Compression

A universal tension-compression testing machine was used for individual-panel axial compression

buckling tests to obtain additional room-temperature buckling data in pure compression. Figure 15 shows the test machine with a test panel mounted. A total of 11 displacement transducers (DT's) were used to measure the out-of-plane deformations of the test panel.

The surfaces of the upper and lower platens (which come into direct contact with the panel ends) were machined flat to ensure pure compression loading and to eliminate possible bending because of misaligned platen surfaces. The lower platen rested on a spherical seat and provided proper alignment with the test panel.

End supports mounted on the panel provided surfaces for load transfer and served as reinforcement for the elimination of warping of the panel ends. The surfaces of both end supports were milled parallel with each other and perpendicular to the panel tube axes to provide pure compression load transfer.

The panel vertical edges were bolted to the z-section stiffeners to approximate the stiffness conditions of a wing-mounted support. The interface between the panel and the stiffeners was lubricated. The holes on the stiffeners were oval shaped so that the bolts could move when the panel deformed.

Strain Gage Instrumentation

The strain gage locations on the surfaces of the five test panels are shown in figure 16. The view in the figure is looking downward from the top of the test panels. The strain gages with parentheses were located on the upper surfaces of the panels, and the rosette strain gages with square brackets were used for the elevated-temperature tests. The strain gages on the upper and lower surfaces of the panel tubes were single axial strain gages of two types: (1) foil type (circular symbol) and (2) capacitance type (square symbol). Of the axial strain gages, only the capacitance strain gages were capable of operating at temperatures above 550°F. The strain gages on the surface of the panel flat areas were the delta-rosette foil type and are indicated by the triangles in figure 16. At temperatures above 550°F, the bonded rosette gages were replaced with welded gages which are capable of operating at a temperature of 1200°F. The delta-rosette strain gages were used to make measurements at three angular orientations spaced 120° apart starting in the direction parallel to the wing spars and rotating clockwise (when looking down on the test panels and inboard). The accuracy of the data acquisition system for strain gage measurements was $\pm 5 \times 10^{-6}$, which represents 0.3 percent of the strain gage calibration output. Figure 17 shows the full instrumentation of strain gages and thermocouples on test panel 5, and figure 18

shows the fully instrumented test panels attached to the HWTS lower wing root test area with panel 3 removed to show the pressure pan interior.

For the elevated-temperature tests, the strain gage outputs were corrected by subtracting the initial nonzero readings at temperature without mechanical load. Figure 19 shows the strain produced when the weldable gages are welded to René 41 and heated. This apparent strain would totally account for the initial nonzero reading if no gage drift or strain due to thermal stress exists. These initial readings were generally of the magnitude shown in figure 19, indicating that gage drift and thermal stress were small. Figure 20 shows the full instrumentation of strain gages on the outer surface of test panel 1 for room-temperature, pure-compression, single-panel buckling tests.

Test Procedure

Combined Load Tests

To generate a wide range of buckling data, a series of nondestructive buckling tests using the F/S method was conducted under various combined load conditions and at three temperatures (70°F (room temperature), 550°F, and 1000°F). Table 2 shows the maximum loads applied at the load points for different load conditions. Before the series of tests at 70°F, the pressure system was checked to assure that a constant pressure level could be maintained during the tests. The pressure load was always maintained at the constant level of 0.75 psi or at 0 psi. Before the elevated-temperature tests, the heating system was checked to assure that constant temperature levels could be maintained over one test period. During the combined load, elevated-temperature tests, heat was first applied to raise the HWTS wing panels to a uniform temperature, and then pressure and mechanical loads were applied in that order. Table 3 shows the test numbers and the corresponding load conditions.

Compression Tests

Because the nondestructive buckling tests failed to produce results in pure compression at room temperature with $p = 0$ psi (see *Results and Discussion*), two panels (panels 1 and 3) were tested to buckling failure at that load condition in a universal tension-compression testing machine. During the tests, the signals from the load cell, strain gage, and deflectionometer channels were fed into the data acquisition system so that F/S plots could be generated. The buckling loads obtained from the F/S plots could then be compared with the actual buckling loads.

Data Reduction

In applying the F/S method mentioned previously, a typical vertical load (lift force) F_{703} located at load point 703 (associated with jack number 3; see fig. 11) was selected as F in equation (16) (or fig. 7) in the F/S calculations for all the test panels. The load F_{703} was arbitrarily selected as a representative measurement of all applied loads since all loads were directly proportional to each other and were applied simultaneously. For $F = F_{703}$, equation (22) becomes

$$k = \frac{F_{cr}}{F^*} = \frac{(F_{703})_{cr}}{F_{703}^*} \quad (25)$$

where $(F_{703})_{cr}$ is the value of F_{703} at the predicted buckling point and F_{703}^* is the maximum value of F_{703} in the nondestructive buckling test. The buckling values of the panel stress resultants $(N_x)_{cr}$ and $(N_{xy})_{cr}$ may be calculated by using equations (20), (21), (23), (24), and (25). For example, for panel 1 at room temperature with strain gage combination RSG 933, RSG 934, and RSG 935 (see fig. 16), equations (20) and (21) may be written as

$$N_x^* = E\bar{t}[(RSG^* 933) - 0] \quad (26)$$

$$N_{xy}^* = \frac{4}{\sqrt{3}}Gt|[(RSG^* 934) - 0] - [(RSG^* 935) - 0]| \quad (27)$$

and $(N_x)_{cr}$ and $(N_{xy})_{cr}$ can be calculated from equations (23) and (24) as follows:

$$(N_x)_{cr} = kN_x^* = \frac{(F_{703})_{cr}}{F_{703}^*} N_x^* \quad (28)$$

$$(N_{xy})_{cr} = kN_{xy}^* = \frac{(F_{703})_{cr}}{F_{703}^*} N_{xy}^* \quad (29)$$

Results and Discussion

Combined Loads

Figures 21, 22, and 23 show respectively the force/stiffness (F/S) plots for the three typical tests 4.2.6 ($p = 0.75$ psi), 4.4.6 ($p = 0.75$ psi), and 4.3.4 ($p = 0$ psi) at 70°F. The solid curves shown in the figures were drawn from least-squares fits of the test data points. For some tests, or for certain strain gage combinations in the same test, the least-squares-fit curves based on equation (17) started to bend upward immediately after the last data points and intersected with the limit strain lines at points predicting rather high values of the buckling loads. For such occurrences, the extrapolations of the test data curves were accomplished by visually fitting the

data. No attempt was made to improve the extrapolations by modifying equation (17) or by excluding data at low loads from the data set used to define the least-squares fit. The dashed curves shown in the three plots in figures 21(a), 21(c), and 21(d) were drawn as visual extrapolations. Notice that the plot in figure 21(b) shows excellent extrapolation of the least-squares-fit curve. With the existence of the lateral pressure ($p = 0.75$ psi), the F/S plots are usually convex upward. (See figs. 21 and 22.) However, when there is no lateral pressure ($p = 0$ psi), the F/S plots usually give strong convex downward curves except for the low-load region, giving quite accurate buckling load predictions (see fig. 23). The F/S plots for the rest of the tests where buckling loads are predicted are similar and therefore are not shown.

Compression

Figure 24 shows panel 3 after the room-temperature single-panel compression buckling test. A loud popping sound and a noticeable drop in load occurred at buckling. On one side of the panel, local failures (bead crippling) were observed at three of the four beads within 5 in. of the panel center. (See fig. 24.) Only two small creases on a bead were observed on the other side. None of the strain gages were located directly at a buckle, although one small buckle not visible in figure 24 was located near strain gage 515. The behavior of panel 1 was similar except that buckles occurred in all four beads.

Figure 25 shows out-of-plane displacements of three cross sections of test panel 3 at the panel compression load of $(N_x)_{cr} = 2138$ lbf/in. immediately before buckling. The smaller displacements measured near the panel edges indicate the existence of a stabilizing effect from the edge supports and may explain why the panel did not fail in general buckling at the predicted room-temperature Euler wide-column load of 1684 lbf/in. obtained from reference 6. The local buckling load of 1622 lbf/in., also determined from reference 6, was exceeded by an even greater amount. As discussed subsequently, these results indicate that the theory used to design and analyze these panels appears to be unnecessarily conservative in compression.

Figures 26 and 27 show respectively the F/S plots for panels 3 and 1 for the room-temperature single-panel compression tests. Notice that the actual buckling points are located in the vicinity of the limit strain lines, and a visual extrapolation of the F/S data shown in figure 26(b), which were from strain gages located near a buckle, would give excellent agreement with the failure force of 41 051 lbf. These results indicate that the F/S method could

fairly accurately predict buckling loads in pure compression. (As discussed later, F/S predictions of buckling failure in pure compression at room temperature were not obtained for panels tested in the HWTS (fig. 28(a)) because the applied load was limited to a low value.)

Comparison With Theory

Table 4 summarizes the results of all the tests. In the table, N_x^* and N_{xy}^* are associated with F_{703}^* and $(N_x)_{cr}$ and $(N_{xy})_{cr}$ with $(F_{703})_{cr}$. For most tests, the extrapolation factor $k = (F_{703})_{cr}/F_{703}^*$ was between 2 and 3, thus indicating relatively large extrapolations. The large extrapolations were necessary because the applied loads were limited to less than 50 percent of the wing panel buckling load to prevent failure of the spar flanges, which were, by design, the critical components of the HWTS.

The results given in table 4 were used to construct the buckling interaction plots shown in figure 28 for different temperatures with or without pressure. The theoretical buckling interaction curves shown in the figures for comparison were generated through temperature and material modulus corrections of the results given in table 1 of reference 6. The two curves shown for local buckling were plotted with and without the additional knockdown factor of 0.86 for equation (5).

For high compression (see fig. 28(b)), the maximum applied loads were not large enough to give accurate buckling data through the F/S data extrapolations. Nevertheless, the correlations between the test data and the predictions are fairly good in spite of data scatter resulting from the large extrapolations for some tests (e.g., near the N_x -axis). Most of the data points, including the actual buckling points obtained from the single-panel compression tests (see fig. 28(a)), fall outside the predicted interaction curves, indicating the theoretical results are conservative. (As previously mentioned, these results are based on a thickness of 0.016 in. and include effects from an assumed 0.001L initial imperfection). In all other tests, the theoretical curves fall within the scatter of the experimental data. Therefore, the experimental buckling data verify the theory for the applied test conditions and indicate that the additional knockdown factor of 0.86 for local buckling in compression recommended in reference 6 is not necessary.

As would be expected, the existence of lateral pressure, which adds a bending stress to the compression stress, decreases the compression buckling load $(N_x)_{cr}$ considerably, but only slightly decreases the shear buckling load $(N_{xy})_{cr}$. Also, the buckling interaction curve shrinks as the temperature

is increased because of the decreases in E and G . Finally, the room-temperature pure-compression buckling loads per unit panel weight $(N_x)_{cr}/w$ ($w = 0.0161 \text{ lbm/in}^2$) for the tubular panels 1 and 3 are $1.5067 \times 10^5 \text{ in.}$ and $1.3280 \times 10^5 \text{ in.}$, respectively. These values are slightly higher than $(N_x)_{cr}/w = 1.1507 \times 10^5 \text{ in.}$ ($w = 0.0146 \text{ lbm/in}^2$) reported in reference 9 for the René 41 beaded panels which were originally used on the HWTS.

Conclusions

Five René 41 tubular panels which show promise of low structural mass and high buckling strength were installed as replacement root-chord wing panels on a section of a hot hypersonic wing test structure. To characterize their buckling behavior, the panels were exposed to nondestructive buckling tests under different combined load conditions and different temperature environments representative of those which would be encountered in a hot hypersonic wing, except that the structure was maintained at uniform temperatures. Thus, the results included the effect of changes in modulus with temperature while the complex thermal stresses which can arise when temperatures are not uniform were minimized. Buckling loads for the wide range of loads and temperatures were obtained without failing the test panels through use of the force/stiffness method.

In spite of some data scattering because of large extrapolations, the overall test data correlated fairly well with theoretically predicted buckling interaction curves. The existence of lateral pressure added a bending stress to the compression stress and thereby decreased the compression buckling load $(N_x)_{cr}$ considerably. However, the effect of the lateral pressure on the reduction of the shear buckling load $(N_{xy})_{cr}$ was quite small. Also, increasing the temperature decreased both $(N_x)_{cr}$ and $(N_{xy})_{cr}$ because of reductions in the shear modulus and the modulus of elasticity at elevated temperatures. The fact that almost all the test data for nearly pure compression at room temperature fell outside the predicted buckling interaction curves indicates that the theory used to design and predict the buckling of the panels is conservative for that condition. For all other test conditions, the force/stiffness test data verified the theory and showed that the structural efficiency of the tubular panel is slightly higher than that of the beaded panel which it replaced.

References

1. Plank, P. P.; Sakata, I. F.; Davis, G. W.; and Richie, C. C.: *Hypersonic Cruise Vehicle Wing Structure Evaluation*. NASA CR-1568, 1970.
2. Greene, Bruce E.: *Substantiation Data for Advanced Beaded and Tubular Structural Panels—Volume 1, Design and Analysis*. NASA CR-132460, [1974].
3. Musgrove, Max D.; and Northrop, Russell F.: *Substantiation Data for Advanced Beaded and Tubular Structural Panels—Volume 2, Fabrication*. NASA CR-132482, [1974].
4. Hedges, Phillip C.; and Greene, Bruce E.: *Substantiation Data for Advanced Beaded and Tubular Structural Panels—Volume 3, Testing*. NASA CR-132515, [1974].
5. Musgrove, Max D.; and Greene, Bruce E.: *Advanced Beaded and Tubular Structural Panels*. NASA CR-2514, 1975.
6. Greene, Bruce E.; and Northrop, Russell F.: *Design and Fabrication of René 41 Advanced Structural Panels*. NASA CR-132646, [1975].
7. Musgrove, Max D.; Greene, Bruce E.; Shideler, John L.; and Bohon, Herman L.: Advanced Beaded and Tubular Structural Panels. *J. Aircr.*, vol. 11, no. 2, Feb. 1974, pp. 68–75.
8. Shideler, John L.; Bohon, Herman L.; and Greene, Bruce E.: Evaluation of Bead-Stiffened Metal Panels. AIAA Paper No. 75-815, May 1975.
9. Siegel, William H.: *Experimental and Finite Element Investigation of the Buckling Characteristics of a Beaded Skin Panel for a Hypersonic Aircraft*. NASA CR-144863, 1978.
10. Shideler, John L.; Fields, Roger A.; and Reardon, Lawrence F.: Tests of Beaded and Tubular Structural Panels. *Recent Advances in Structures for Hypersonic Flight*, NASA CP-2065, Part II, 1978, pp. 539–576.
11. Jones, Robert E.; and Greene, Bruce E.: The Force/Stiffness Technique for Nondestructive Buckling Testing. *A Collection of Technical Papers—AIAA/ASME/SAE 15th Structures, Structural Dynamics and Materials Conference*, Apr. 1974. (Available as AIAA Paper 74-351.)
12. Plank, P. P.; and Penning, F. A.: *Hypersonic Wing Test Structure Design, Analysis, and Fabrication*. NASA CR-127490, 1973.
13. Fields, Roger A.; Reardon, Lawrence F.; and Siegel, William H.: *Loading Tests of a Wing Structure for a Hypersonic Aircraft*. NASA TP-1596, 1980.
14. *Metallic Materials and Elements for Aerospace Vehicle Structures. Volume 1*. MIL-HDBK-5B, U.S. Dep. Defense, Sept. 1, 1971.

NASA Langley Research Center
Hampton, VA 23665-5225
August 1, 1986

Table 1. Material Properties and Theoretical Local Buckling Strains for René 41

Parameter	Values for temperatures of—		
	70°F	550°F	1000°F
E , psi	31.6×10^6	29.1×10^6	26.5×10^6
G , psi	12.1×10^6	11.2×10^6	10.2×10^6
f_{cy} , psi	125.0×10^3	120.0×10^3	117.0×10^3
$(\epsilon_c)_{cr}$	$2.330 \times 10^{-3}(\eta_3 = 1)$	$2.330 \times 10^{-3}(\eta_3 = 1)$	$2.330 \times 10^{-3}(\eta_3 = 1)$
$(\epsilon_b)_{cr}$	$3.412 \times 10^{-3}(\eta_3 = 0.96)$	$3.412 \times 10^{-3}(\eta_3 = 0.97)$	$3.412 \times 10^{-3}(\eta_3 = 0.99)$
γ_{cr}	$2.208 \times 10^{-3}(\eta_2 = 1)$	$2.208 \times 10^{-3}(\eta_2 = 1)$	$2.208 \times 10^{-3}(\eta_2 = 1)$

Table 2. Jack Loads Applied to HWTS for Different Load Conditions
(a) $T = 70^\circ\text{F}$

Jack	Jack position	Maximum load, ^a lbf, for load condition—						
		3.1	3.6	3.8	4.1	4.2	4.3	4.4
1	Vertical	1680	2521	4 201	3500	2800	1200	-4000
2	Vertical	867	1304	2 173	6000	2800	2000	2400
3	Vertical	624	735	1 557	6000	2800	2000	2400
4	Vertical	863	1274	2 157	3500	2800	-2800	-4000
5	Horizontal		1650	2 750		-5000	-5000	-5000
6	Horizontal		4260	7 100		-6500	-6500	-6500
7	Horizontal		-4030	-6 716		6500	6500	6500
8	Horizontal		-1232	-2 054		6500	6500	6500
9	Horizontal		-3840	-6 350		6000	6000	6000
10	Horizontal		731	1 227		6000	6000	6000
11	Vertical	2265	3398	5 663	3000	800	-800	-4000
12	Vertical	-95	-193	-238	1800	1400	1200	1200
13	Horizontal		-6692	-11 154		6500	6500	6500
14	Horizontal		-3945	-6 575		6500	6500	6500
15	Horizontal		-1740	-2 900		-6500	-6500	-6500
16	Horizontal		2400	4 000		-6500	-6500	-6500
17	Vertical	1267	1901	3 168	3500	2800	2800	4000
18	Vertical	-1896	-2770	-4 616	3500	4800	4800	4000
19	Vertical	1760	3640	4 400	2800	2800	2500	4000
20	Vertical	592	814	1 356	1800	1400	1200	1200

^aPositive values indicate tension; negative values indicate compression.

Table 2. Continued

(b) $T = 550^{\circ}\text{F}$

Jack	Jack position	Maximum load, ^a lbf, for load condition—					
		6.6	6.8	7.1	7.2	7.3	7.4
1	Vertical	2 521	4 201	3500	2800	1200	-4000
2	Vertical	1 304	2 173	6000	2800	2000	2900
3	Vertical	735	1 559	6000	2800	2000	2400
4	Vertical	1 294	2 157	3500	2800	-2800	-4000
5	Horizontal	1 650	2 750		-5000	-5000	-5000
6	Horizontal	4 260	7 100		-6500	-6500	-6500
7	Horizontal	-11 030	-6 716		6500	6500	6500
8	Horizontal	-1 232	-2 054		6500	6500	6500
9	Horizontal	-3 840	-6 350		6000	6000	6000
10	Horizontal	737	1 227		6000	6000	6000
11	Vertical	3 398	5 663	3000	800	-800	-4000
12	Vertical	-143	-238	1800	1400	1200	1200
13	Horizontal	-6 692	-11 154		6500	6500	6500
14	Horizontal	-3 945	-6 575		6500	6500	6500
15	Horizontal	-1 740	-2 700		-6500	-6500	-6500
16	Horizontal	2 400	4 000		-6500	-6500	-6500
17	Vertical	1 901	3 168	3300	2800	2800	4000
18	Vertical	-2 770	-4 616	3500	4800	4800	4000
19	Vertical	2 640	4 400	2800	2800	2800	4000
20	Vertical	814	1 356	1800	1400	1200	1200

^aPositive values indicate tension; negative values indicate compression.

Table 2. Concluded

(c) $T = 1000^{\circ}\text{F}$

Jack	Jack position	Maximum load, ^a lbf, for load condition—					
		9.3	9.5	8.1	8.2	8.3	8.4
1	Vertical	2 521	4 201	3500	2800	1200	-4000
2	Vertical	1 304	2 173	6000	2500	2000	2400
3	Vertical	935	1 559	6000	2800	2000	2400
4	Vertical	1 294	2 157	3500	2800	-2800	-4000
5	Horizontal	1 650	2 750		-5000	-5000	-5000
6	Horizontal	4 260	7 100		-6500	-6500	-6500
7	Horizontal	-4 030	-6 716		6500	6500	6500
8	Horizontal	-1 232	-2 054		6500	6500	6500
9	Horizontal	-3 840	-6 350		6000	6000	6000
10	Horizontal	737	1 229		6000	6000	6000
11	Vertical	3 398	5 663	3000	800	-800	-4000
12	Vertical	-143	-238	1800	1400	1200	1200
13	Horizontal	-6 672	-11 154		6500	6500	6500
14	Horizontal	-3 945	-6 575		6500	6500	6500
15	Horizontal	-1 740	-2 700		-6500	-6500	-6500
16	Horizontal	2 400	4 000		-6500	-6500	-6500
17	Vertical	1 901	3 168	3500	2800	2800	4000
18	Vertical	-2 770	-4 616	3500	4800	4800	4000
19	Vertical	2 640	4 400	2800	2800	2800	4000
20	Vertical	814	1 356	1800	1400	1200	1200

^aPositive values indicate tension; negative values indicate compression.

Table 3. Test Numbers and Corresponding Load Conditions

Test	Load condition	Pressure, psi	Temperature, °F
4.1.4	4.1	0.75	70
4.2.6	4.2	.75	70
4.3.3	4.3	.75	70
4.4.6	4.4	.75	70
4.2.7	4.2	0	70
4.3.4	4.3	0	70
4.4.7	4.4	0	70
6.8.3	3.8	.75	550
7.2.4	4.2	.75	550
7.3.5	4.3	.75	550
7.4.4	4.4	.75	550
7.1.8	4.1	.75	550
8.2.2	4.2	0	1000
8.2.2	4.2	.75	1000
8.3.2	4.3	0	1000
8.3.2	4.3	.75	1000
8.3.5	4.3	0	1000
8.3.5	4.3	.75	1000
8.4.6	4.4	0	1000
8.4.6	4.4	.75	1000
8.1.3	4.1	0	1000
8.1.3	4.1	.75	1000
Single-panel test 1.1	(a)	0	70
Single-panel test 3.1	(a)	0	70

^a $N_x \neq 0; N_{xy} = 0$.

Table 4. Summary of Test Results

Test	Panel	Location (a)	Strain gage combinations for equations (18) to (21)	Maximum measured values of—		F/S predicted values of—			
				N_x^* , lbf/in.	N_{xy}^* , lbf/in.	N_x^*/N_x^*	N_{xy}^*/N_{xy}^*	$(N_x)_{cr}$, lbf/in.	$(N_{xy})_{cr}$, lbf/in.
4.1.4 $T = 70^\circ F$ $p = 0.75$ psi	1	1	504, 505, 933, 934, 935	615	28	0.05	2.91	1790	82
			502, 503, 933, 934, 935						
	2	2	500, 501, 927, 928, 929	757	1	0	$b_{2.74}$	2074	3
			426, 427, 927, 928, 929						
	2	1	510, 511, 948, 949, 950	551	55	0.10	2.90	1598	160
			508, 509, 948, 949, 950						
	2	2	506, 507, 942, 943, 944	723	70	0.10	2.09	1511	146
			435, 436, 942, 943, 944						
	3	1	516, 517, 963, 964, 965	641	26	0.04	$b_{2.60}$	1667	68
			514, 515, 963, 964, 965						
	2	2	512, 513, 957, 958, 959	754	19	0.03	$b_{2.78}$	2196	70
			534, 535, 957, 958, 959						
	4	1	522, 523, 978, 979, 980	636	11	0.02	$b_{2.64}$	1679	29
			520, 521, 978, 979, 980						
	2	2	518, 519, 972, 973, 974	744	3	0	$b_{2.83}$	2106	8
			603, 604, 972, 973, 974						
	5	1	528, 529, 993, 994, 995	637	75	0.12	$b_{2.69}$	2001	8
			526, 527, 993, 994, 995						
	2	2	524, 525, 987, 988, 989	743	55	0.07	$b_{2.78}$	2066	153

^aLocation 1—half-panel location; location 2—quarter-panel location.

^bFrom visual extrapolation of F/S data.

Table 4. Continued

Test	Panel	Location (a)	Strain gage combinations for equations (18) to (21)	Maximum measured values of—			F/S predicted values of—		
				N_x^* , lbf/in.	N_{xy}^* , lbf/in.	N_{xy}^*/N_x^*	$(N_x)_{cr}$, lbf/in.	$(N_{xy})_{cr}$, lbf/in.	
4.2.6 $T = 70^\circ\text{F}$ $p = 0.75$ psi	1	1	504, 505, 933, 934, 935	362	194	0.54	2.24	811	435
			502, 503, 933, 934, 935	416	207	0.50	^b 2.19	793	425
	2	2	500, 501, 927, 928, 929	309	204	0.66	2.58	1073	534
			426, 427, 927, 928, 929	438	192	0.44	2.32	965	480
	1	1	510, 511, 948, 949, 950	510	287	0.56	2.25	695	459
			508, 509, 948, 949, 950	582	283	0.49	2.17	671	443
	2	2	506, 507, 942, 943, 944	529	267	0.51	^b 2.47	1082	474
			435, 436, 942, 943, 944	787	217	0.28	2.79	1222	536
	3	1	516, 517, 963, 964, 965	510	287	0.56	^b 1.97	1005	565
			514, 515, 963, 964, 965	582	283	0.49	1.87	954	537
	2	2	512, 513, 957, 958, 959	529	267	0.51	^b 1.97	1147	558
			534, 535, 957, 958, 959	529	267	0.51	^b 1.93	1123	546
	4	1	522, 523, 978, 979, 980	628	250	0.40	2.25	1190	601
			520, 521, 978, 979, 980	628	250	0.40	2.14	1132	571
	2	2	518, 519, 972, 973, 974	633	266	0.42	2.35	1476	588
			603, 604, 972, 973, 974	633	266	0.42	2.53	1589	633
	5	1	528, 529, 993, 994, 995	787	217	0.28	1.90	1203	505
			526, 527, 993, 994, 995	787	217	0.28	2.15	1361	572
2	2	524, 525, 987, 988, 989	787	217	0.28	^b 2.02	1590	438	

^aLocation 1—half-panel location; location 2—quarter-panel location.

^bFrom visual extrapolation of F/S data.

Table 4. Continued

Test	Panel	Location (a)	Strain gage combinations for equations (18) to (21)	Maximum measured values of—			F/S predicted values of—		
				N_x^* , lbf/in.	N_{xy}^* , lbf/in.	N_{xy}^*/N_x^*	k	$(N_x)_{cr}$, lbf/in.	$(N_{xy})_{cr}$, lbf/in.
4.3.3 $T = 70^\circ\text{F}$ $p = 0.75$ psi	1	1	504, 505, 933, 934, 935	214	261	1.23	b 2.25	482	587
			502, 503, 933, 934, 935						
	2	2	500, 501, 927, 928, 929	225	267	1.19	2.42	518	632
			426, 427, 927, 928, 929						
	2	1	510, 511, 948, 949, 950	123	286	2.33	2.09	257	598
			508, 509, 948, 949, 950						
	3	2	506, 507, 942, 943, 944	203	276	1.36	2.03	412	560
			435, 436, 942, 943, 944						
	4	1	516, 517, 963, 964, 965	285	366	1.28	b 1.89	539	692
			514, 515, 963, 964, 965						
	5	2	512, 513, 957, 958, 959	320	364	1.14	1.85	527	677
			534, 535, 957, 958, 959						
	6	1	522, 523, 978, 979, 980	317	329	1.04	1.81	579	659
			520, 521, 978, 979, 980						
	7	2	518, 519, 972, 973, 974	320	313	0.978	1.82	582	662
			603, 604, 972, 973, 974						
	8	1	528, 529, 993, 994, 995	324	300	0.926	b 2.29	733	717
			526, 527, 993, 994, 995						
	9	2	524, 525, 987, 988, 989	436	256	0.587	2.25	729	675
						2.76	1210	707	

^aLocation 1—half-panel location; location 2—quarter-panel location.

^bFrom visual extrapolation of F/S data.

Table 4. Continued

Test	Panel	Location (a)	Strain gage combinations for equations (18) to (21)	Maximum measured values of—			F/S predicted values of—		
				N_x^* , lbf/in.	N_{xy}^* , lbf/in.	N_{xy}^*/N_x^*	k	$(N_x)_{cr}$, lbf/in.	$(N_{xy})_{cr}$, lbf/in.
4.4.6 $T = 70^\circ\text{F}$ $p = 0.75$ psi	1	1	504, 505, 933, 934, 935	126	342	2.71	^b 2.20	277	752
				502, 503, 933, 934, 935	114	341	2.99	2.28	287
	2	2	500, 501, 927, 928, 929	7	380	54.3	2.44	278	832
				426, 427, 927, 928, 929	65	379	5.83	^b 2.18	249
	2	1	510, 511, 948, 949, 950	65	379	5.83	2.05	14	779
				508, 509, 948, 949, 950	143	460	3.22	2.08	15
	3	1	506, 507, 942, 943, 944	144	459	3.19	2.04	133	773
				435, 436, 942, 943, 944	144	459	3.19	2.00	130
	4	1	516, 517, 963, 964, 965	111	417	3.76	1.65	236	759
				514, 515, 963, 964, 965	142	402	2.83	1.61	230
	5	1	512, 513, 957, 958, 959	141	357	2.53	1.71	246	785
				534, 535, 957, 958, 959	230	311	1.35	1.59	229
	5	2	522, 523, 978, 979, 980	111	417	3.76	1.93	214	805
				520, 521, 978, 979, 980	142	402	2.83	1.83	203
	5	1	518, 519, 972, 973, 974	141	357	2.53	2.03	288	816
				603, 604, 972, 973, 974	141	357	2.53	2.04	290
	5	2	528, 529, 993, 994, 995	141	357	2.53	1.99	281	710
				526, 527, 993, 994, 995	230	311	1.35	^b 2.10	296
5	1	524, 525, 987, 988, 989	230	311	1.35	2.44	561	759	
			524, 525, 987, 988, 989	230	311	1.35	2.44	561	759

^aLocation 1—half-panel location; location 2—quarter-panel location.

^bFrom visual extrapolation of F/S data.

Table 4. Continued

Test	Panel	Strain gage combinations for equations (18) to (21)	Maximum measured values of—			F/S predicted values of—	
			N_x^* , lbf/in.	N_{xy}^* , lbf/in.	N_{xy}^*/N_x^*	$(N_x)_{cr}$, lbf/in.	$(N_{xy})_{cr}$, lbf/in.
4.2.7 $T = 70^\circ\text{F}$ $p = 0 \text{ psi}$	1	504, 505, 616, 617, 618	406	185	0.456		
		502, 503, 616, 617, 618					
		500, 501, 616, 617, 618					
		426, 427, 616, 617, 618					
		510, 511, 619, 620, 621					
	2	508, 509, 619, 620, 621	340	211	0.621		
		506, 507, 619, 620, 621					
		435, 436, 619, 620, 621					
		516, 517, 622, 623, 624					
		514, 515, 622, 623, 624					
	3	512, 513, 622, 623, 624	570	291	0.511		
		534, 535, 622, 623, 624					
		522, 523, 634, 635, 636					
		520, 521, 634, 635, 636					
		518, 519, 634, 635, 636					
4	603, 604, 634, 635, 636	518	252	0.486			
	528, 529, 637, 638, 639						
	526, 527, 637, 638, 639						
	524, 525, 637, 638, 639						
	524, 525, 637, 638, 639						
5	528, 529, 637, 638, 639	609	228	0.374			
	526, 527, 637, 638, 639						
	524, 525, 637, 638, 639						
	524, 525, 637, 638, 639						
	524, 525, 637, 638, 639						

^aLocation 1—half-panel location; location 2—quarter-panel location.

^bFrom visual extrapolation of F/S data.

Table 4. Continued

Test	Panel	Strain gage combinations (18) to (21)	Maximum measured values of—			F/S predicted values of—	
			N_x^* , lbf/in.	N_{xy}^* , lbf/in.	N_{xy}^*/N_x^*	$(N_x)_{cr}$, lbf/in.	$(N_{xy})_{cr}$, lbf/in.
4.3.4 $T = 70^\circ\text{F}$ $p = 0$ psi	1	504, 505, 616, 617, 618	243	276	1.14	^b 2.71	659
		502, 503, 616, 617, 618				2.83	688
		500, 501, 616, 617, 618				2.72	661
	2	426, 427, 616, 617, 618				2.69	654
		510, 511, 619, 620, 621	169	298	1.76	2.26	382
		508, 509, 619, 620, 621				2.11	357
	3	506, 507, 619, 620, 621				2.13	360
		435, 436, 619, 620, 621				2.34	395
		516, 517, 622, 623, 624	319	389	1.22	1.81	577
		514, 515, 622, 623, 624				1.81	577
	4	512, 513, 622, 623, 624				1.83	584
		534, 535, 622, 623, 624				1.70	542
		522, 523, 634, 635, 636	252	322	1.28	1.99	501
		520, 521, 634, 635, 636				2.23	562
		518, 519, 634, 635, 636				2.26	570
5	603, 604, 634, 635, 636						
	528, 529, 637, 638, 639	320	276	0.863	2.58	826	
	526, 527, 637, 638, 639				2.51	803	
		524, 525, 637, 638, 639			2.54	813	

^aLocation 1—half-panel location; location 2—quarter-panel location.

^bFrom visual extrapolation of F/S data.

Table 4. Continued

Test	Panel	Strain gage combinations for equations (18) to (21)	Maximum measured values of—		N_{xy}^* , lbf/in.	N_{xy}^*/N_x^*	k	F/S predicted values of—	
			N_x^* , lbf/in.	N_{xy}^* , lbf/in.				$(N_x)_{cr}$, lbf/in.	$(N_{xy})_{cr}$, lbf/in.
4.4.7 $T = 70^\circ\text{F}$ $p = 0$ psi	1	504, 505, 616, 617, 618	175	353	2.02	2.28	399	805	
		502, 503, 616, 617, 618				1.57	275	554	
		500, 501, 616, 617, 618				2.01	352	710	
		426, 427, 616, 617, 618				2.40	420	847	
	2	510, 511, 619, 620, 621	63	393	6.24	1.81	114	711	
		508, 509, 619, 620, 621				1.80	113	707	
		506, 507, 619, 620, 621				2.00	126	786	
		435, 436, 619, 620, 621				^b 1.99	125	783	
	3	516, 517, 622, 623, 624	182	496	2.73	1.52	277	754	
		514, 515, 622, 623, 624				1.54	280	764	
		512, 513, 622, 623, 624				1.57	286	779	
		534, 535, 622, 623, 624				1.48	269	734	
	4	522, 523, 634, 635, 636	97	413	4.26	1.77	172	731	
		520, 521, 634, 635, 636				1.89	183	781	
		518, 519, 634, 635, 636				1.90	184	785	
		603, 604, 634, 635, 636							
5	528, 529, 637, 638, 639	158	338	2.14	2.02	319	683		
	526, 527, 637, 638, 639				2.22	351	750		
	524, 525, 637, 638, 639				2.09	330	706		

^aLocation 1—half-panel location; location 2—quarter-panel location.

^bFrom visual extrapolation of F/S data.

Table 4. Continued

Test	Panel	Strain gage combinations for equations (18) to (21)	Maximum measured values of—			F/S predicted values of—		
			N_x^* , lbf/in.	N_{xy}^* , lbf/in.	N_{xy}^*/N_x^*	$(N_x)_{cr}$, lbf/in.	$(N_{xy})_{cr}$, lbf/in.	
6.8.3 $T = 550^\circ\text{F}$ $p = 0.75$ psi	1	504, 505, 616, 617, 618	122	137	1.12	$b_{4.59}$	560	629
		502, 503, 616, 617, 618					580	651
		500, 501, 616, 617, 618					520	584
		426, 427, 616, 617, 618					600	674
	2	510, 511, 619, 620, 621	226	182	0.81	$b_{3.89}$	879	708
		508, 509, 619, 620, 621					551	444
		506, 507, 619, 620, 621					509	410
		435, 436, 619, 620, 621					741	597
	3	516, 517, 622, 623, 624	305	147	0.48	$b_{2.79}$	851	410
		514, 515, 622, 623, 624					949	457
		512, 513, 622, 623, 624					979	472
		534, 535, 622, 623, 624					900	434
	4	522, 523, 634, 635, 636	299	155	0.52	$b_{3.52}$	1052	546
		520, 521, 634, 635, 636					930	482
		518, 519, 634, 635, 636					1029	533
		603, 604, 634, 635, 636						
	5	528, 529, 637, 638, 639	407	100	0.25	$b_{2.95}$	1201	295
		526, 527, 637, 638, 639					1091	268
		524, 525, 637, 638, 639					1351	332

^aLocation 1—half-panel location; location 2—quarter-panel location.

^bFrom visual extrapolation of F/S data.

Table 4. Continued

Test	Panel	Strain gage combinations for equations (18) to (21)	Maximum measured values of—			F/S predicted values of—	
			N_x^* , lbf/in.	N_{xy}^* , lbf/in.	N_x^*/N_x	$(N_x)_{cr}$, lbf/in.	$(N_{xy})_{cr}$, lbf/in.
7.2.4 $T = 550^\circ\text{F}$ $p = 0.75 \text{ psi}$	1	504, 505, 616, 617, 618	59	209	3.54		
		502, 503, 616, 617, 618					
		500, 501, 616, 617, 618					
	2	426, 427, 616, 617, 618	188	179	0.95		
		510, 511, 619, 620, 621					
		508, 509, 619, 620, 621					
	3	506, 507, 619, 620, 621	358	262	0.73		
		435, 436, 619, 620, 621					
		516, 517, 622, 623, 624					
	4	514, 515, 622, 623, 624	330	232	0.70		
		512, 513, 622, 623, 624					
		534, 535, 622, 623, 624					
	5	522, 523, 634, 635, 636	495	188	0.38		
		520, 521, 634, 635, 636					
		518, 519, 634, 635, 636					
	603, 604, 634, 635, 636						
	528, 529, 637, 638, 639						
	526, 527, 637, 638, 639						
		524, 525, 637, 638, 639					

^aLocation 1—half-panel location; location 2—quarter-panel location.

^bFrom visual extrapolation of F/S data.

Table 4. Continued

Test	Panel	Strain gage combinations for equations (18) to (21)	Maximum measured values of—			F/S predicted values of—					
			N_x^* , lbf/in.	N_{xy}^* , lbf/in.	N_{xy}^*/N_x^*	k	$(N_x)_{cr}$, lbf/in.	$(N_{xy})_{cr}$, lbf/in.			
7.3.5 $T = 550^\circ\text{F}$ $p = 0.75$ psi	1	504, 505, 616, 617, 618	10	263	26.3	$b_{2.87}$	29	755			
		502, 503, 616, 617, 618							$b_{2.92}$	29	768
		500, 501, 616, 617, 618							$b_{3.19}$	32	839
		426, 427, 616, 617, 618				$b_{3.06}$	31	805			
	2	510, 511, 619, 620, 621	48	249	5.20	2.92	140	727			
		508, 509, 619, 620, 621							$b_{3.06}$	147	762
		506, 507, 619, 620, 621							3.33	160	829
	3	435, 436, 619, 620, 621	173	342	1.98	2.92	140	727			
		516, 517, 622, 623, 624							$b_{2.13}$	368	728
		514, 515, 622, 623, 624							$b_{2.07}$	358	708
	4	512, 513, 622, 623, 624	124	295	2.38	2.02	349	691			
		534, 535, 622, 623, 624							1.91	330	653
		522, 523, 634, 635, 636							3.13	388	923
	5	520, 521, 634, 635, 636	215	234	1.09	2.76	342	814			
		518, 519, 634, 635, 636							2.92	362	861
603, 604, 634, 635, 636											
	528, 529, 637, 638, 639				$b_{2.92}$	628	683				
	526, 527, 637, 638, 639				$b_{3.19}$	686	746				
	524, 525, 637, 638, 639				$b_{3.06}$	658	716				

^aLocation 1—half-panel location; location 2—quarter-panel location.

^bFrom visual extrapolation of F/S data.

Table 4. Continued

Test	Panel	Strain gage combinations for equations (18) to (21)	Maximum measured values of—			N_x^*/N_x^*	k	F/S predicted values of—						
			N_x^* , lbf/in.	N_{xy}^* , lbf/in.	N_{xy}^*/N_x^*			$(N_x)_{cr}$, lbf/in.	$(N_{xy})_{cr}$, lbf/in.					
7.4.4 $T = 550^\circ\text{F}$ $p = 0.75 \text{ psi}$	1	504, 505, 616, 617, 618	136	321	2.36	2.27	309	729						
		502, 503, 616, 617, 618							2.19	298	703			
		500, 501, 616, 617, 618										2.54	345	815
		426, 427, 616, 617, 618												
	510, 511, 619, 620, 621	2.14	79	740										
	508, 509, 619, 620, 621				2.20	81	761							
	506, 507, 619, 620, 621							2.26	84	782				
	435, 436, 619, 620, 621										2.16	80	747	
	516, 517, 622, 623, 624	1.68	311	721										
	514, 515, 622, 623, 624				1.65	305	708							
	512, 513, 622, 623, 624							1.75	324	751				
	534, 535, 622, 623, 624										1.66	307	712	
	522, 523, 634, 635, 636	2.16	134	791										
	520, 521, 634, 635, 636				2.14	133	783							
	518, 519, 634, 635, 636							2.26	140	827				
	603, 604, 634, 635, 636										2.55	293	752	
	528, 529, 637, 638, 639	2.46	283	726										
	526, 527, 637, 638, 639				2.65	305	782							
	524, 525, 637, 638, 639													

Table 4. Continued

Test	Panel	Strain gage combinations for equations (18) to (21)	Maximum measured values of—			F/S predicted values of—		
			N_x^* , lbf/in.	N_{xy}^* , lbf/in.	N_{xy}^*/N_x^*	k	$(N_x)_{cr}$, lbf/in.	$(N_{xy})_{cr}$, lbf/in.
7.1.8 $T = 550^\circ\text{F}$ $p = 0.75$ psi	1	504, 505, 616, 617, 618	185	9	0.05	$b_{5.68}$	1051	51
		502, 503, 616, 617, 618						
		500, 501, 616, 617, 618						
		426, 427, 616, 617, 618						
		510, 511, 619, 620, 621						
	2	508, 509, 619, 620, 621	374	60	0.16	$b_{2.94}$	1100	176
		506, 507, 619, 620, 621						
		435, 436, 619, 620, 621						
		516, 517, 622, 623, 624						
	3	514, 515, 622, 623, 624	448	8	0.02	$b_{2.85}$	1277	23
		512, 513, 622, 623, 624						
		534, 535, 622, 623, 624						
		522, 523, 634, 635, 636						
	4	520, 521, 634, 635, 636	440	2	0.00	$b_{3.03}$	1333	6
		518, 519, 634, 635, 636						
603, 604, 634, 635, 636								
5	528, 529, 637, 638, 639	507	24	0.05	$b_{2.37}$	1202	57	
	526, 527, 637, 638, 639							
	524, 525, 637, 638, 639							

^aLocation 1—half-panel location; location 2—quarter-panel location.

^bFrom visual extrapolation of F/S data.

Table 4. Continued

Test	Panel	Strain gage combinations for equations (18) to (21)	Maximum measured values of—			F/S predicted values of—		
			N_x^* , lbf/in.	N_{xy}^* , lbf/in.	N_x^*/N_x^*	k	$(N_x)_{cr}$, lbf/in.	$(N_{xy})_{cr}$, lbf/in.
8.2.2 $T = 1000^\circ\text{F}$ $p = 0$ psi	1	504, 505, 616, 617, 618	274	122	0.45	3.78	1036	461
		502, 503, 616, 617, 618						
		500, 501, 616, 617, 618						
	2	510, 511, 619, 620, 621	219	148	0.68	2.46 ^b	539	364
		508, 509, 619, 620, 621						
		506, 507, 619, 620, 621						
	3	516, 517, 622, 623, 624	358	142	0.40	2.75	985	391
		514, 515, 622, 623, 624						
		512, 513, 622, 623, 624						
		522, 523, 634, 635, 636						
	4	520, 521, 634, 635, 636	343	173	0.50	2.91 ^b	998	503
		518, 519, 634, 635, 636						
		528, 529, 637, 638, 639						
	5	526, 527, 637, 638, 639	402	157	0.39	2.62	1053	411
		524, 525, 637, 638, 639						

^aLocation 1—half-panel location; location 2—quarter-panel location.

^bFrom visual extrapolation of F/S data.

Table 4. Continued

Test	Panel	Strain gage combinations for equations (18) to (21)	Maximum measured values of —			F/S predicted values of —		
			N_x^* , lbf/in.	N_{xy}^* , lbf/in.	N_{xy}^*/N_x^*	$(N_x)_{cr}$, lbf/in.	$(N_{xy})_{cr}$, lbf/in.	
8.2.2 $T = 1000^\circ\text{F}$ $p = 0.75$ psi	1	504, 505, 616, 617, 618	181	128	0.71	4.13	748	529
		502, 503, 616, 617, 618						
		500, 501, 616, 617, 618						
	2	510, 511, 619, 620, 621	160	130	0.81	$b_{3.45}$	552	449
		508, 509, 619, 620, 621						
		506, 507, 619, 620, 621						
	3	516, 517, 622, 623, 624	260	209	0.80	$b_{2.74}$	712	573
		514, 515, 622, 623, 624						
		512, 513, 622, 623, 624						
	4	522, 523, 634, 635, 636	248	168	0.68	$b_{2.76}$	684	464
		520, 521, 634, 635, 636						
		518, 519, 634, 635, 636						
	5	528, 529, 637, 638, 639	356	151	0.42	$b_{2.30}$	819	347
		526, 527, 637, 638, 639						
		524, 525, 637, 638, 639						

^aLocation 1—half-panel location; location 2—quarter-panel location.

^bFrom visual extrapolation of F/S data.

Table 4. Continued

Test	Panel	Strain gage combinations for equations (18) to (21)	Maximum measured values of—			k	F/S predicted values of—	
			N_x^* , lbf/in.	N_{xy}^* , lbf/in.	N_{xy}^*/N_x^*		$(N_x)_{cr}$, lbf/in.	$(N_{xy})_{cr}$, lbf/in.
8.3.2 $T = 1000^\circ\text{F}$ $p = 0$ psi	1	504, 505, 616, 617, 618	188	165	0.88	3.56	669	587
		502, 503, 616, 617, 618				4.24	797	700
		500, 501, 616, 617, 618				2.56	300	486
	2	510, 511, 619, 620, 621	117	190	1.62	^b 2.97	347	564
		508, 509, 619, 620, 621				2.88	337	547
		506, 507, 619, 620, 621				2.66	625	716
	3	516, 517, 622, 623, 624	235	269	1.14	^b 2.37	557	638
		514, 515, 622, 623, 624				2.39	562	643
		512, 513, 622, 623, 624						
	4	522, 523, 634, 635, 636	212	214	1.01			
		520, 521, 634, 635, 636						
		518, 519, 634, 635, 636						
	5	528, 529, 637, 638, 639	257	191	0.74	^b 2.97	763	567
		526, 527, 637, 638, 639				^b 3.36	864	642
		524, 525, 637, 638, 639				3.88	997	741

^aLocation 1—half-panel location; location 2—quarter-panel location.

^bFrom visual extrapolation of F/S data.

Table 4. Continued

Test	Panel	Strain gage combinations for equations (18) to (21)	Maximum measured values of—			k	F/S predicted values of—	
			N_x^* , lbf/in.	N_{xy}^* , lbf/in.	N_{xy}^*/N_x^*		$(N_x)_{cr}$, lbf/in.	$(N_{xy})_{cr}$, lbf/in.
8.3.2 $T = 1000^\circ\text{F}$ $p = 0.75$ psi	1	504, 505, 616, 617, 618	98	171	1.74	^b 4.22	414	722
		502, 503, 616, 617, 618						
		500, 501, 616, 617, 618						
	2	510, 511, 619, 620, 621	65	175	2.69	2.50	163	438
		508, 509, 619, 620, 621						
		506, 507, 619, 620, 621						
	3	516, 517, 622, 623, 624	159	264	1.66	^b 2.60	413	686
		514, 515, 622, 623, 624						
		512, 513, 622, 623, 624						
	4	522, 523, 634, 635, 636	129	212	1.64	^b 2.64	420	697
		520, 521, 634, 635, 636						
		518, 519, 634, 635, 636						
	5	528, 529, 637, 638, 639	222	185	0.83	^b 2.47	548	457
		526, 527, 637, 638, 639						
		524, 525, 637, 638, 639						

^aLocation 1—half-panel location; location 2—quarter-panel location.

^bFrom visual extrapolation of F/S data.

Table 4. Continued

Test	Panel	Strain gage combinations for equations (18) to (21)	Maximum measured values of—			F/S predicted values of—		
			N_x^* , lbf/in.	N_{xy}^* , lbf/in.	N_{xy}^*/N_x^*	$(N_x)_{cr}$, lbf/in.	$(N_{xy})_{cr}$, lbf/in.	
8.3.5 $T = 1000^\circ\text{F}$ $p = 0$ psi	1	504, 505, 616, 617, 618	179	190	1.06	2.64	473	502
		502, 503, 616, 617, 618						
		500, 501, 616, 617, 618						
	2	510, 511, 619, 620, 621	103	217	2.11	^b 3.10	319	673
		508, 509, 619, 620, 621						
		506, 507, 619, 620, 621						
	3	516, 517, 622, 623, 624	215	298	1.39	2.68	276	582
		514, 515, 622, 623, 624						
		512, 513, 622, 623, 624						
		522, 523, 634, 635, 636						
	4	520, 521, 634, 635, 636	168	236	1.41	2.29	385	540
		518, 519, 634, 635, 636						
		528, 529, 637, 638, 639						
	5	526, 527, 637, 638, 639	221	207	0.94	2.27	488	676
		524, 525, 637, 638, 639						
						^b 2.06	443	614
						^b 2.65	445	625
						2.29	385	540
						^b 2.80	470	661
					^b 2.95	652	611	
					3.14	694	660	
					3.07	678	635	

^aLocation 1—half-panel location; location 2—quarter-panel location.

^bFrom visual extrapolation of F/S data.

Table 4. Continued

Test	Panel	Strain gage combinations for equations (18) to (21)	Maximum measured values of—			k	F/S predicted values of—	
			N_x^* , lbf/in.	N_{xy}^* , lbf/in.	N_{xy}^*/N_x^*		$(N_x)_{cr}$, lbf/in.	$(N_{xy})_{cr}$, lbf/in.
8.3.5 $T = 1000^\circ\text{F}$ $p = 0.75$ psi	1	504, 505, 616, 617, 618	92	217	2.36	^b 3.53	325	766
		502, 503, 616, 617, 618				3.71	341	805
		500, 501, 616, 617, 618				2.41	125	475
	2	510, 511, 619, 620, 621	52	197	3.79	^b 2.94	153	579
		508, 509, 619, 620, 621				2.42	126	477
		506, 507, 619, 620, 621				2.35	282	686
	3	516, 517, 622, 623, 624	120	292	2.43	2.20	264	642
		514, 515, 622, 623, 624				2.29	275	669
		512, 513, 622, 623, 624				^b 3.35	271	791
	4	522, 523, 634, 635, 636	81	236	2.91	^b 2.99	242	706
		520, 521, 634, 635, 636				^b 2.80	227	661
		518, 519, 634, 635, 636				3.36	659	682
	5	528, 529, 637, 638, 639	196	203	1.04	2.87	562	583
		526, 527, 637, 638, 639				3.25	637	660
		524, 525, 637, 638, 639						

^aLocation 1—half-panel location; location 2—quarter-panel location.

^bFrom visual extrapolation of F/S data.

Table 4. Continued

Test	Panel	Strain gage combinations for equations (18) to (21)	Maximum measured values of—			F/S predicted values of—		
			N_x^* , lbf/in.	N_{xy}^* , lbf/in.	N_{xy}^*/N_x^*	$(N_x)_{cr}$, lbf/in.	$(N_{xy})_{cr}$, lbf/in.	
8.4.6 $T = 1000^\circ\text{F}$ $p = 0$ psi	1	504, 505, 616, 617, 618	130	257	1.98	2.27	295	583
		502, 503, 616, 617, 618						
		500, 501, 616, 617, 618						
	2	510, 511, 619, 620, 621	46	289	6.28	2.58	119	746
		508, 509, 619, 620, 621						
		506, 507, 619, 620, 621						
	3	516, 517, 622, 623, 624	146	359	2.46	1.83	267	657
		514, 515, 622, 623, 624						
		512, 513, 622, 623, 624						
	4	522, 523, 634, 635, 636	56	290	5.18	2.36	132	684
		520, 521, 634, 635, 636						
		518, 519, 634, 635, 636						
	5	528, 529, 637, 638, 639	102	249	2.44	2.95	301	735
		526, 527, 637, 638, 639						
		524, 525, 637, 638, 639						

^aLocation 1—half-panel location; location 2—quarter-panel location.

^bFrom visual extrapolation of F/S data.

Table 4. Continued

Test	Panel	Strain gage combinations for equations (18) to (21)	Maximum measured values of—			F/S predicted values of—		
			N_x^* , lbf/in.	N_{xy}^* , lbf/in.	N_{xy}^*/N_x^*	$(N_x)_{cr}$, lbf/in.	$(N_{xy})_{cr}$, lbf/in.	
8.4.6 $T = 1000^\circ\text{F}$ $p = 0.75 \text{ psi}$	1	504, 505, 616, 617, 618	44	258	5.86	$b_{2.45}$	108	632
		502, 503, 616, 617, 618				2.67	117	689
		500, 501, 616, 617, 618				2.69	0	721
	2	510, 511, 619, 620, 621	0	268	∞	2.06	0	552
		508, 509, 619, 620, 621				$b_{2.50}$	0	670
		506, 507, 619, 620, 621				1.86	113	645
	3	516, 517, 622, 623, 624	61	347	5.69	1.94	118	673
		514, 515, 622, 623, 624				2.00	122	694
		512, 513, 622, 623, 624				$b_{2.75}$	0	778
	4	522, 523, 634, 635, 636	0	283	∞	2.82	0	798
		520, 521, 634, 635, 636				2.90	0	821
		518, 519, 634, 635, 636				$b_{3.00}$	222	747
5	528, 529, 637, 638, 639	74	249	3.36	$b_{2.87}$	212	715	
	526, 527, 637, 638, 639							
	524, 525, 637, 638, 639							

^aLocation 1—half-panel location; location 2—quarter-panel location.

^bFrom visual extrapolation of F/S data.

Table 4. Continued

Test	Panel	Strain gage combinations for equations (18) to (21)	Maximum measured values of—			F/S predicted values of—		
			N_x^* , lbf/in.	N_{xy}^* , lbf/in.	N_x^*/N_x^*	$(N_x)_{cr}$, lbf/in.	$(N_{xy})_{cr}$, lbf/in.	
8.1.3 $T = 1000^\circ\text{F}$ $p = 0$ psi	1	504, 505, 616, 617, 618	493	60	0.12			
		502, 503, 616, 617, 618						
		500, 501, 616, 617, 618						
	2	510, 511, 619, 620, 621	408	30	0.07	2.92	1440	175
		508, 509, 619, 620, 621						
		506, 507, 619, 620, 621						
	3	516, 517, 622, 623, 624	484	1	0.002	3.30	1597	3
		514, 515, 622, 623, 624						
		512, 513, 622, 623, 624						
	4	522, 523, 634, 635, 636	459	7	0.02	^b 2.91	1336	20
		520, 521, 634, 635, 636						
		518, 519, 634, 635, 636						
	5	528, 529, 637, 638, 639	445	26	0.06	3.60	1602	94
		526, 527, 637, 638, 639						
		524, 525, 637, 638, 639						

^aLocation 1—half-panel location; location 2—quarter-panel location.

^bFrom visual extrapolation of F/S data.

Table 4. Concluded

Test	Panel	Strain gage combinations for equations (18) to (21)	Maximum measured values of—		k	F/S predicted values of—		
			N_x^* , lbf/in.	N_{xy}^* , lbf/in.		$(N_x)_{cr}$, lbf/in.	$(N_{xy})_{cr}$, lbf/in.	
8.1.3 $T = 1000^\circ\text{F}$ $p = 0.75$ psi	1	504, 505, 616, 617, 618	387	47	0.12	$b_{3.75}$	1451	176
		502, 503, 616, 617, 618				$b_{3.64}$	1409	171
		500, 501, 616, 617, 618				$b_{2.86}$	972	129
	2	510, 511, 619, 620, 621	340	45	0.13	2.28	775	103
		508, 509, 619, 620, 621				2.22	755	100
		506, 507, 619, 620, 621				$b_{3.42}$	1347	7
	3	516, 517, 622, 623, 624	394	2	0.01	$b_{3.52}$	1387	7
		514, 515, 622, 623, 624				$b_{3.30}$	1300	7
		512, 513, 622, 623, 624				3.66	1431	22
	4	522, 523, 634, 635, 636	391	6	0.02	$b_{3.30}$	1290	20
		520, 521, 634, 635, 636				$b_{3.52}$	1376	21
		518, 519, 634, 635, 636				$b_{2.97}$	1197	86
	5	528, 529, 637, 638, 639	403	29	0.07	2.60	1048	75
		526, 527, 637, 638, 639				2.77	1116	80
		524, 525, 637, 638, 639					2426	0
Single panel	1							
	3					2138	0	0

^aLocation 1—half-panel location; location 2—quarter-panel location.

^bFrom visual extrapolation of F/S data.

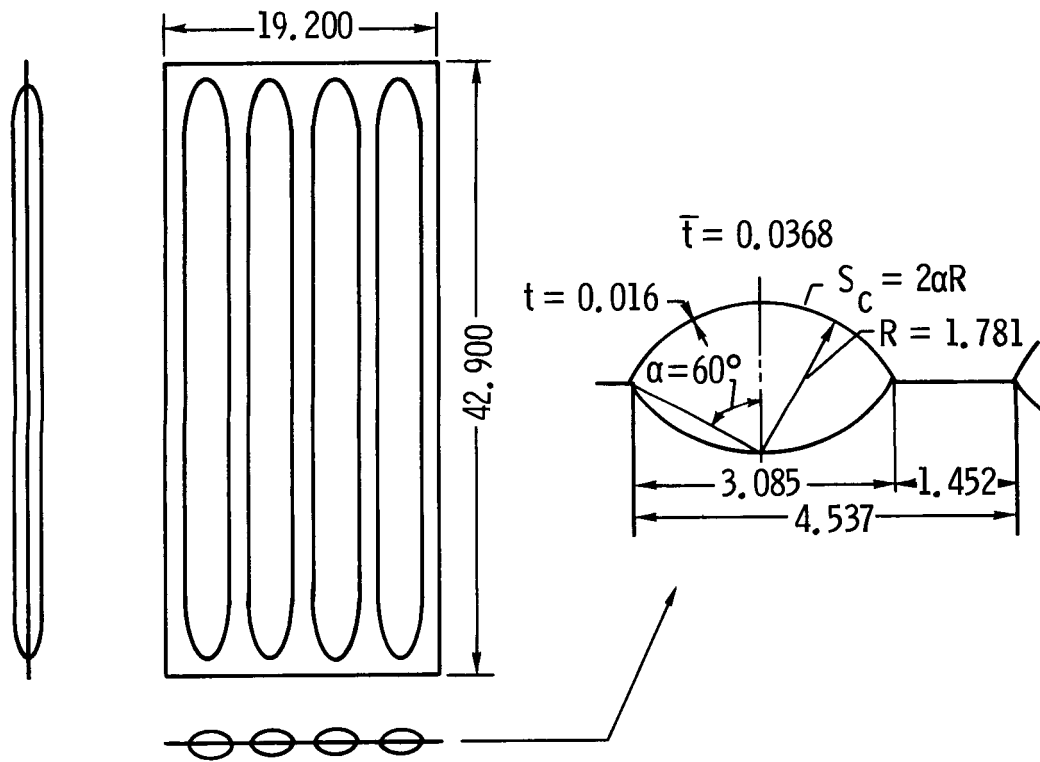
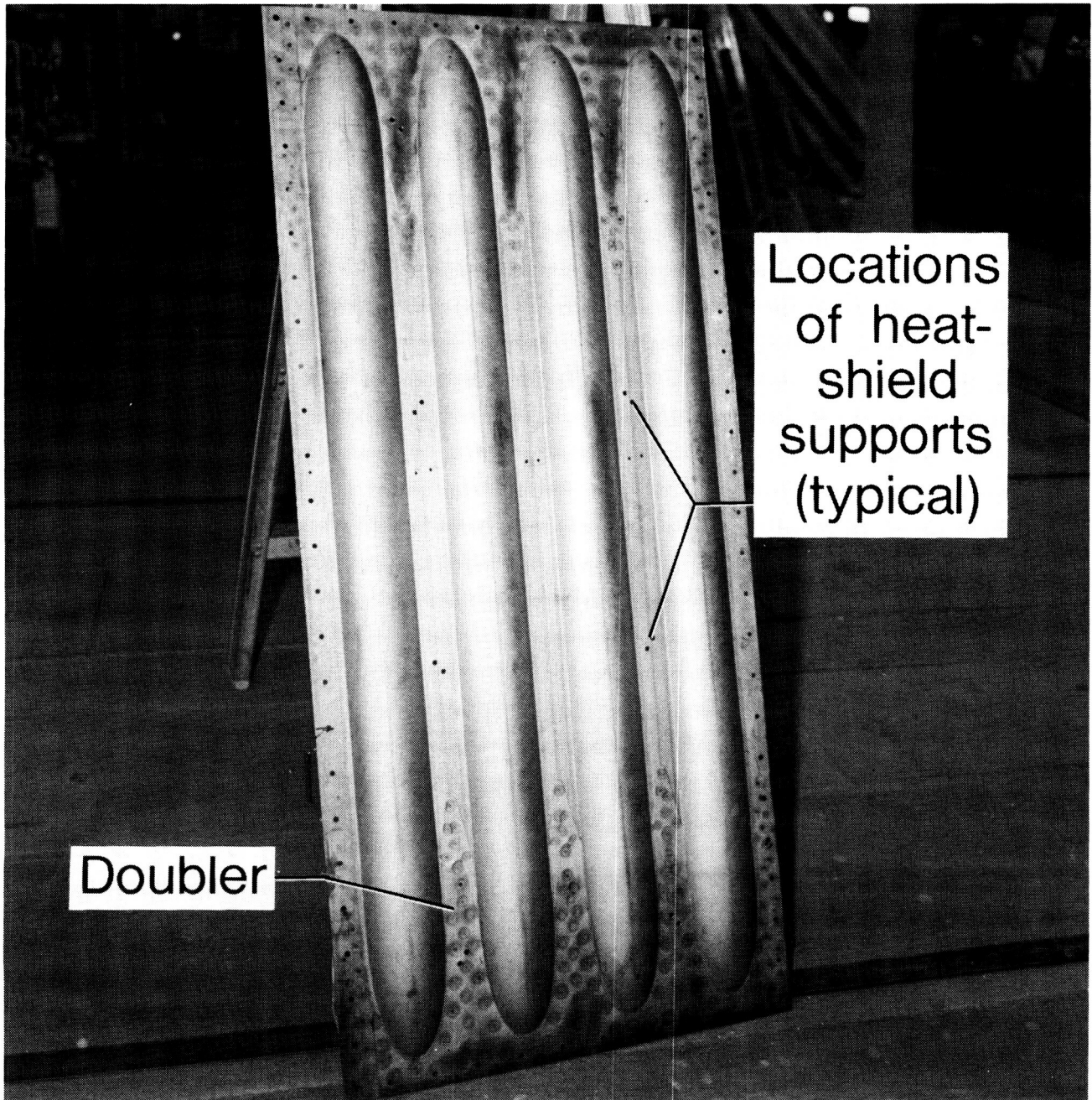


Figure 1. Geometry of tubular panel. Dimensions in inches.



L-86-348

Figure 2. René 41 tubular panel with heat-shield supports removed.

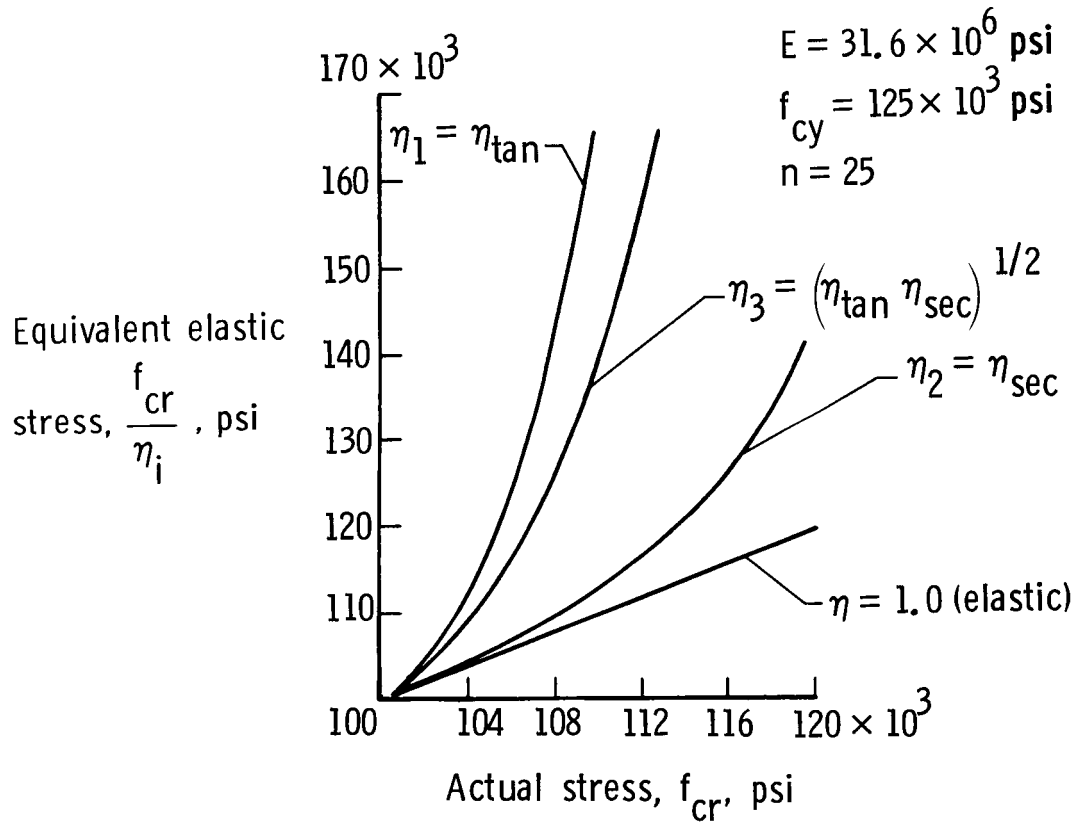


Figure 3. Plasticity correction curves for local buckling of René 41 circular arc element for $T = 70^\circ\text{F}$.

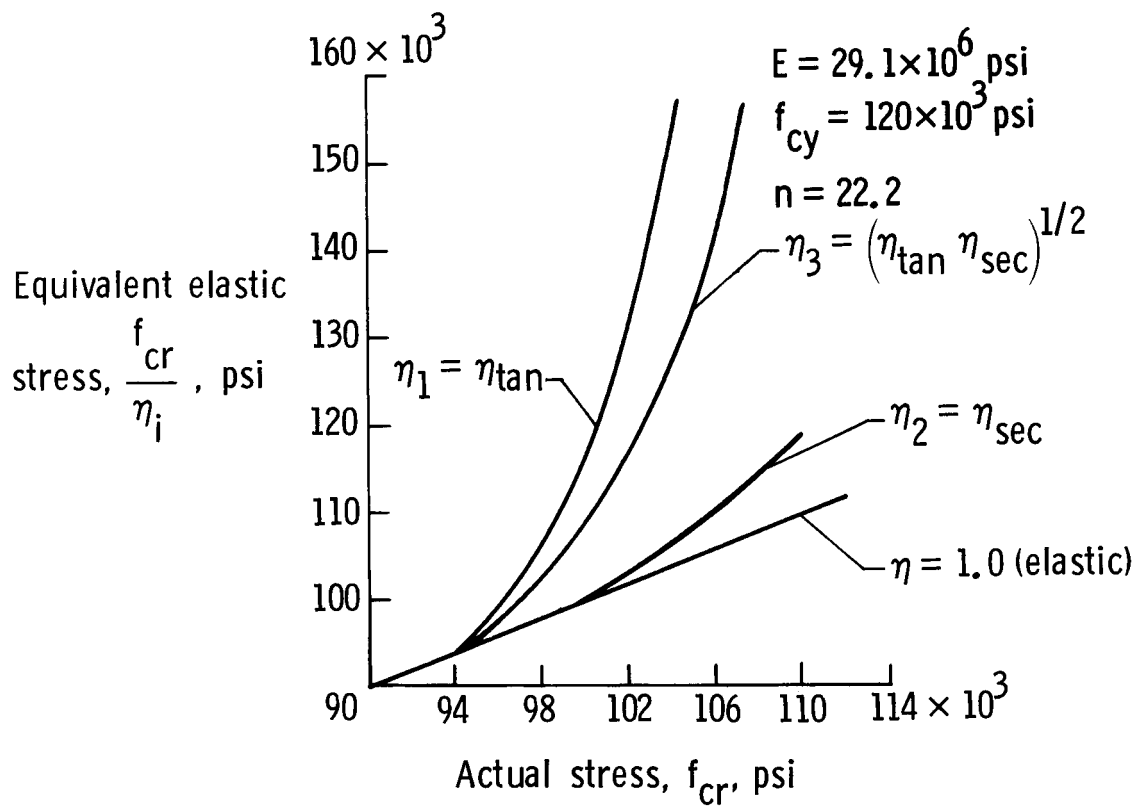


Figure 4. Plasticity correction curves for local buckling of René 41 circular arc element for $T = 550^\circ\text{F}$.

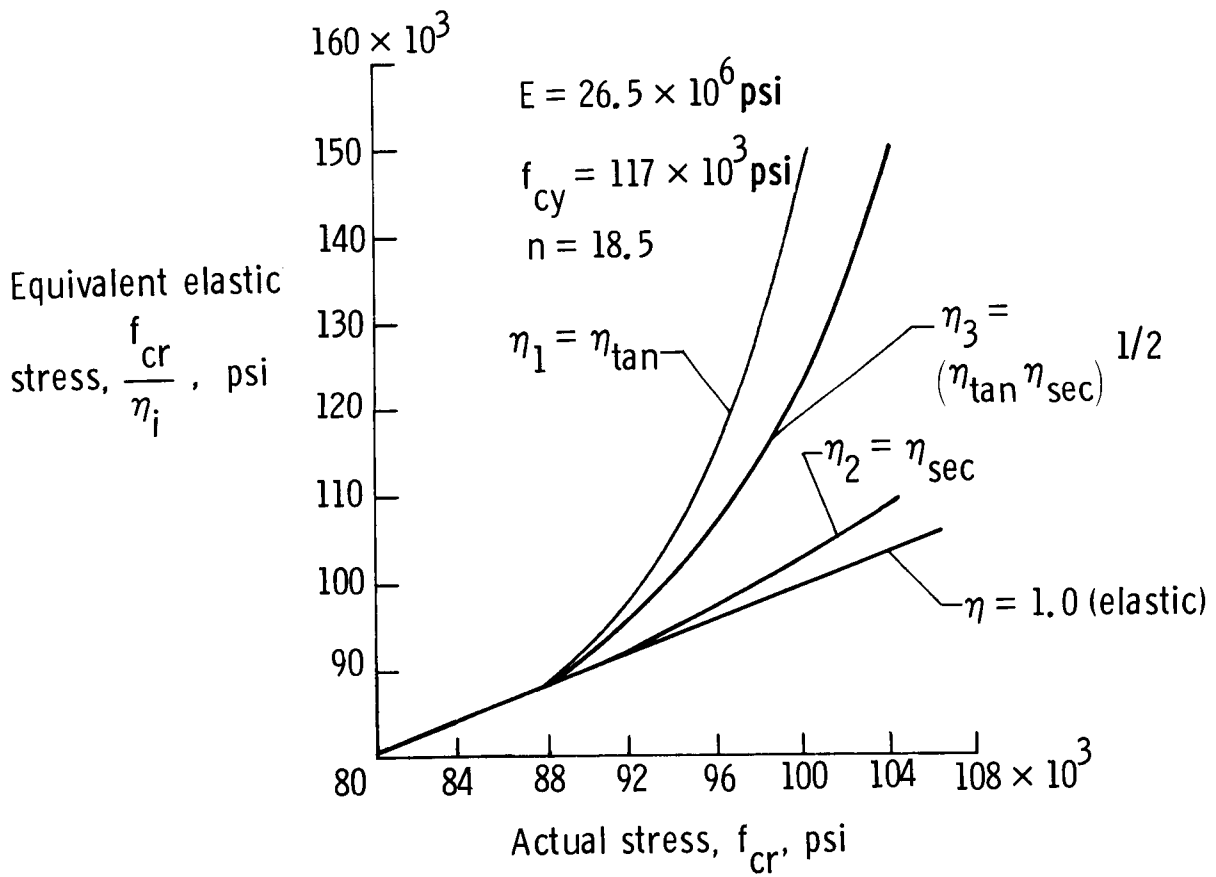


Figure 5. Plasticity correction curves for local buckling of René 41 circular arc element for $T = 1000^\circ\text{F}$.

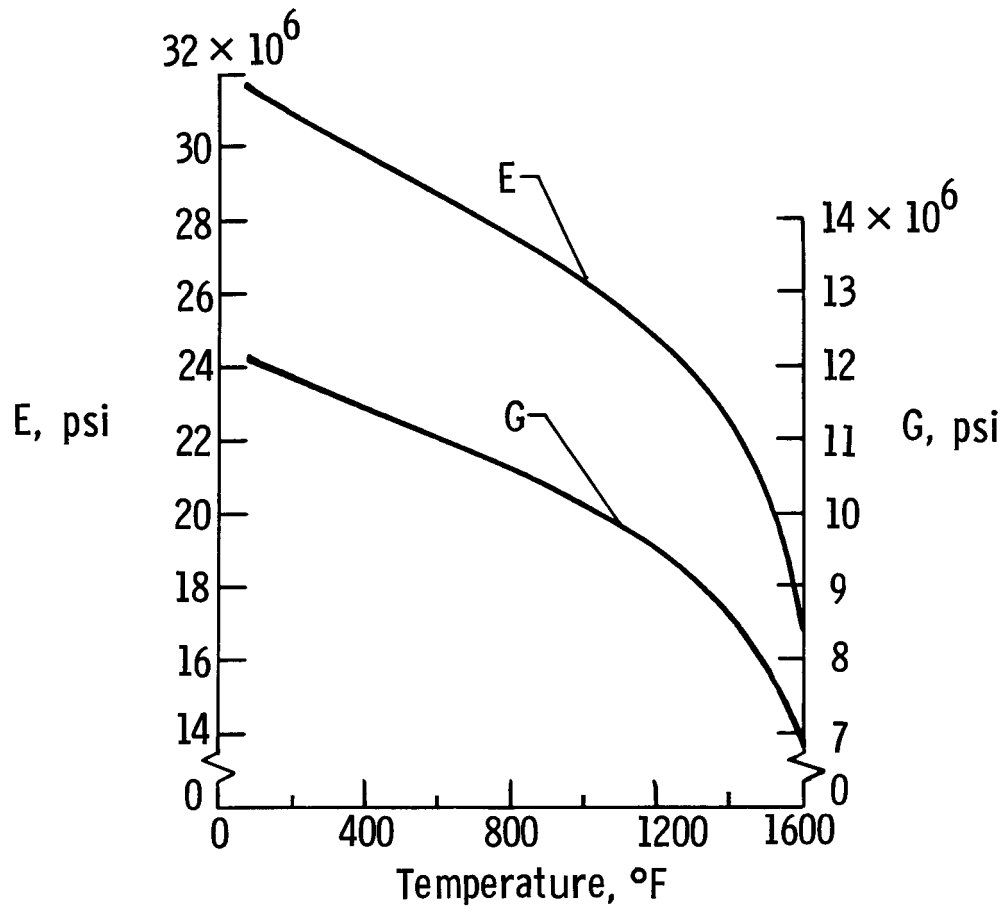


Figure 6. Modulus of elasticity and shear modulus as a function of temperature for René 41.

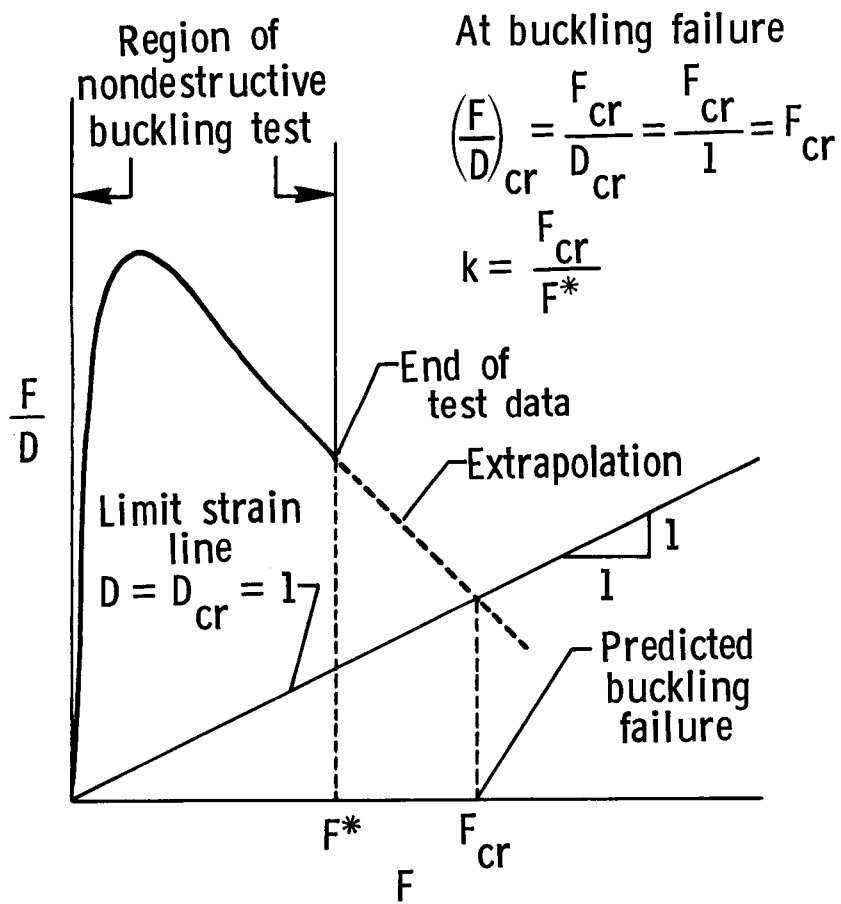
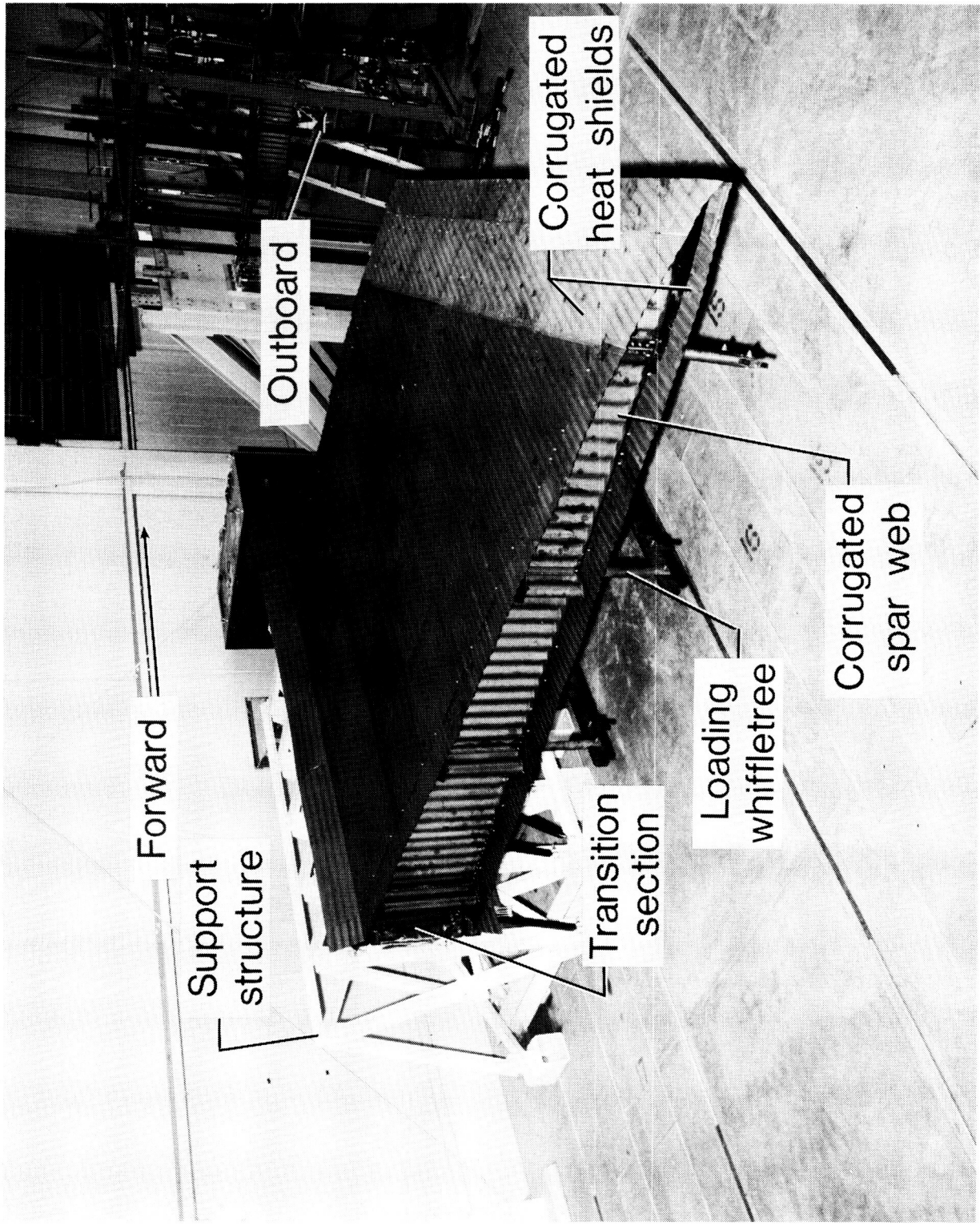
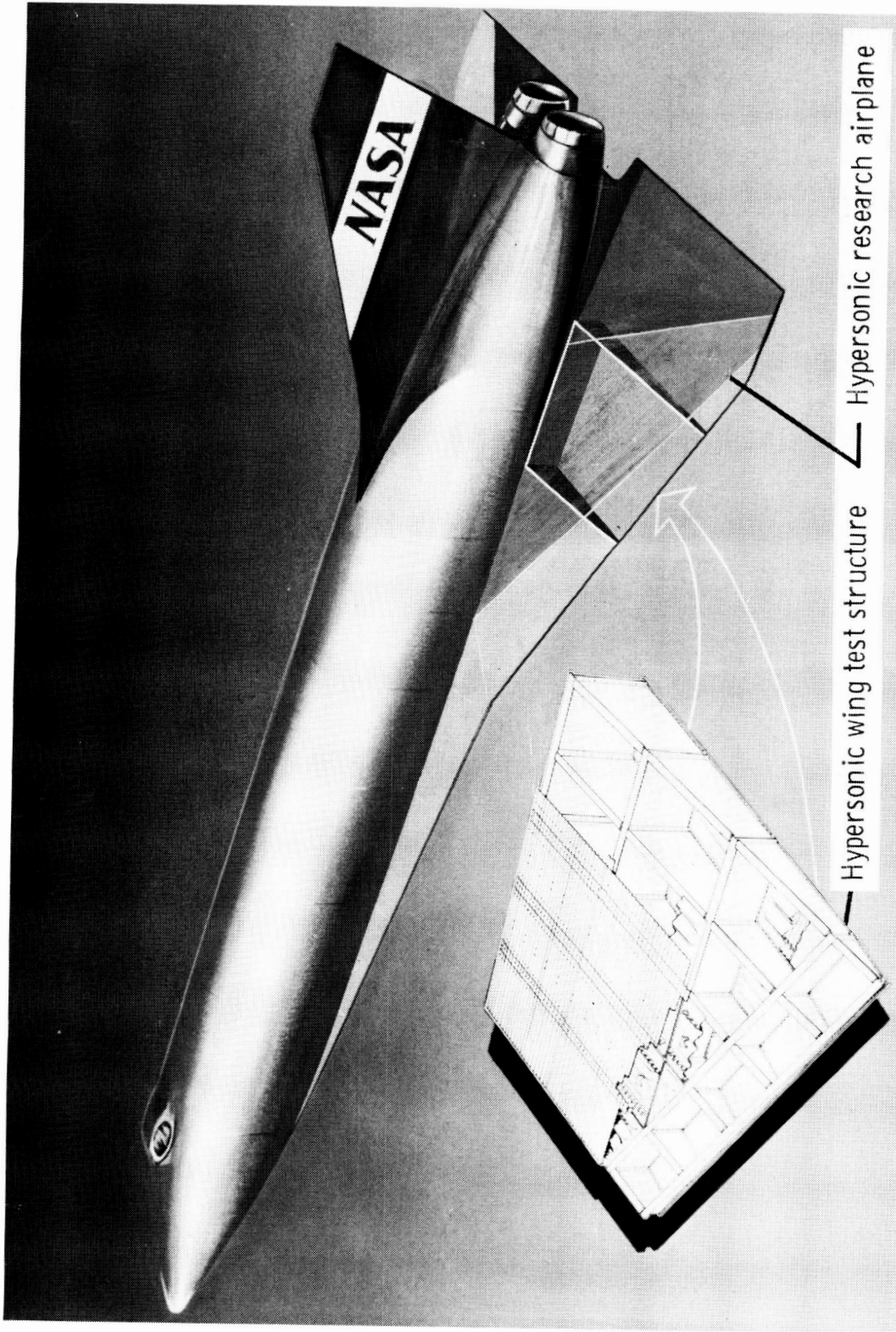


Figure 7. Force/stiffness plot for local buckling.



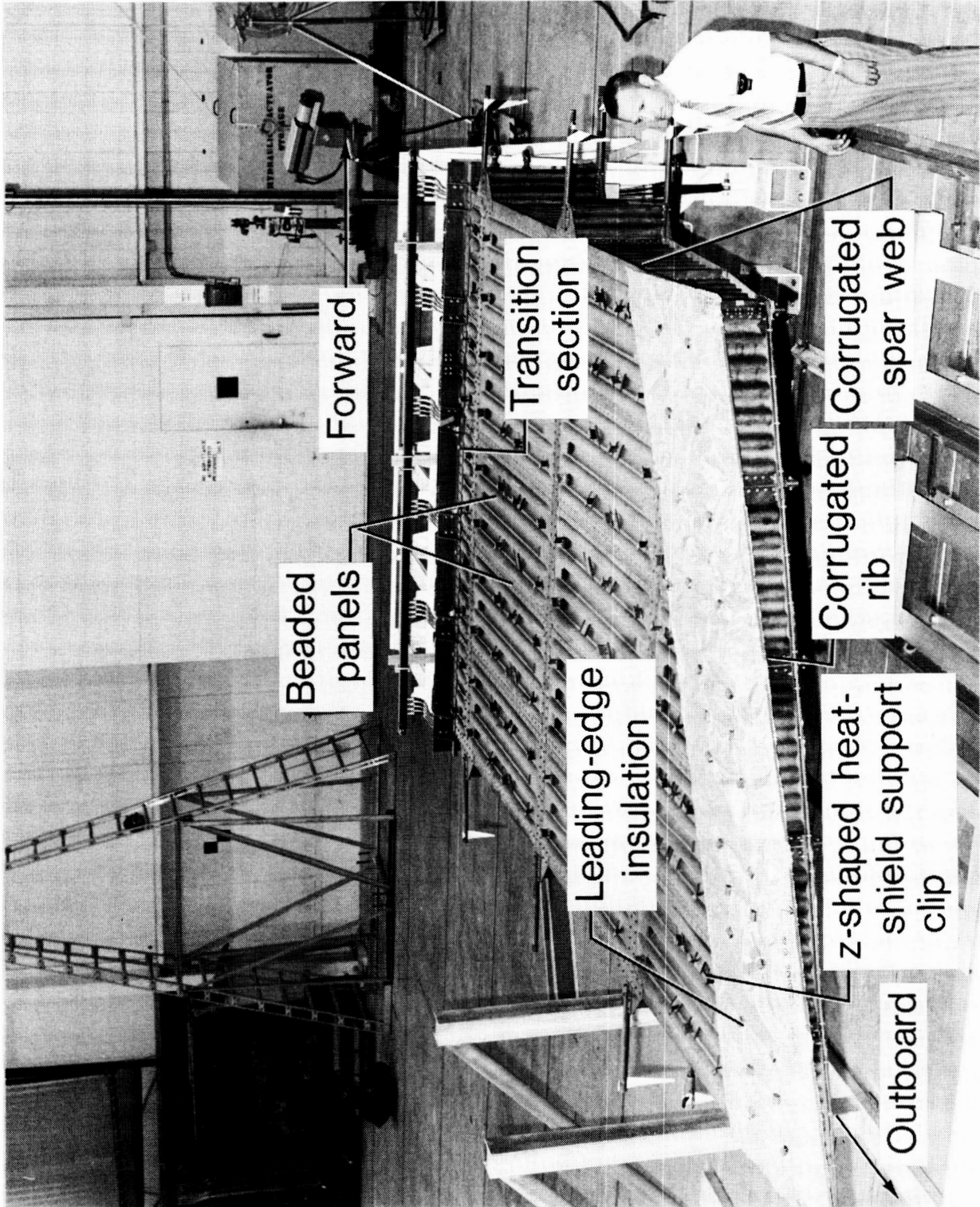
L-86-349

Figure 8. Hypersonic wing test structure (HWTS).



L-86-350

Figure 9. Hypersonic wing test structure as part of hypersonic research airplane.



L-86-351

Figure 10. Hypersonic wing test structure with heat shields removed to show substructure.

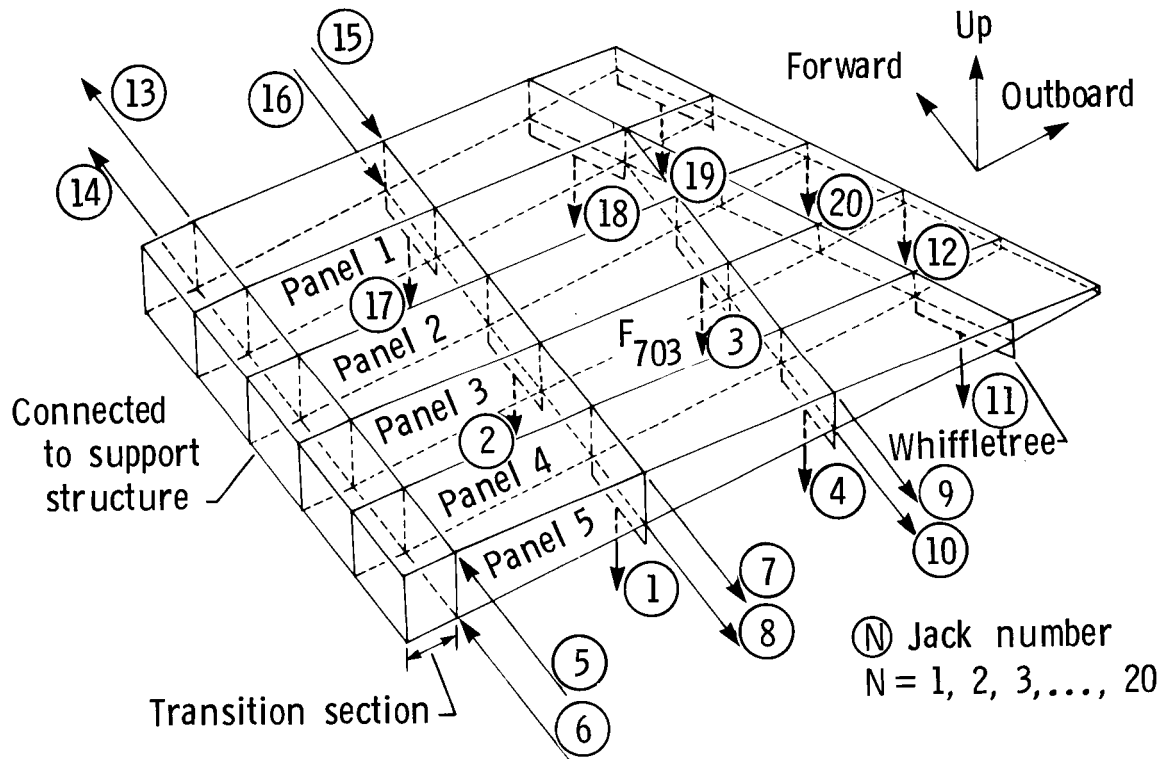
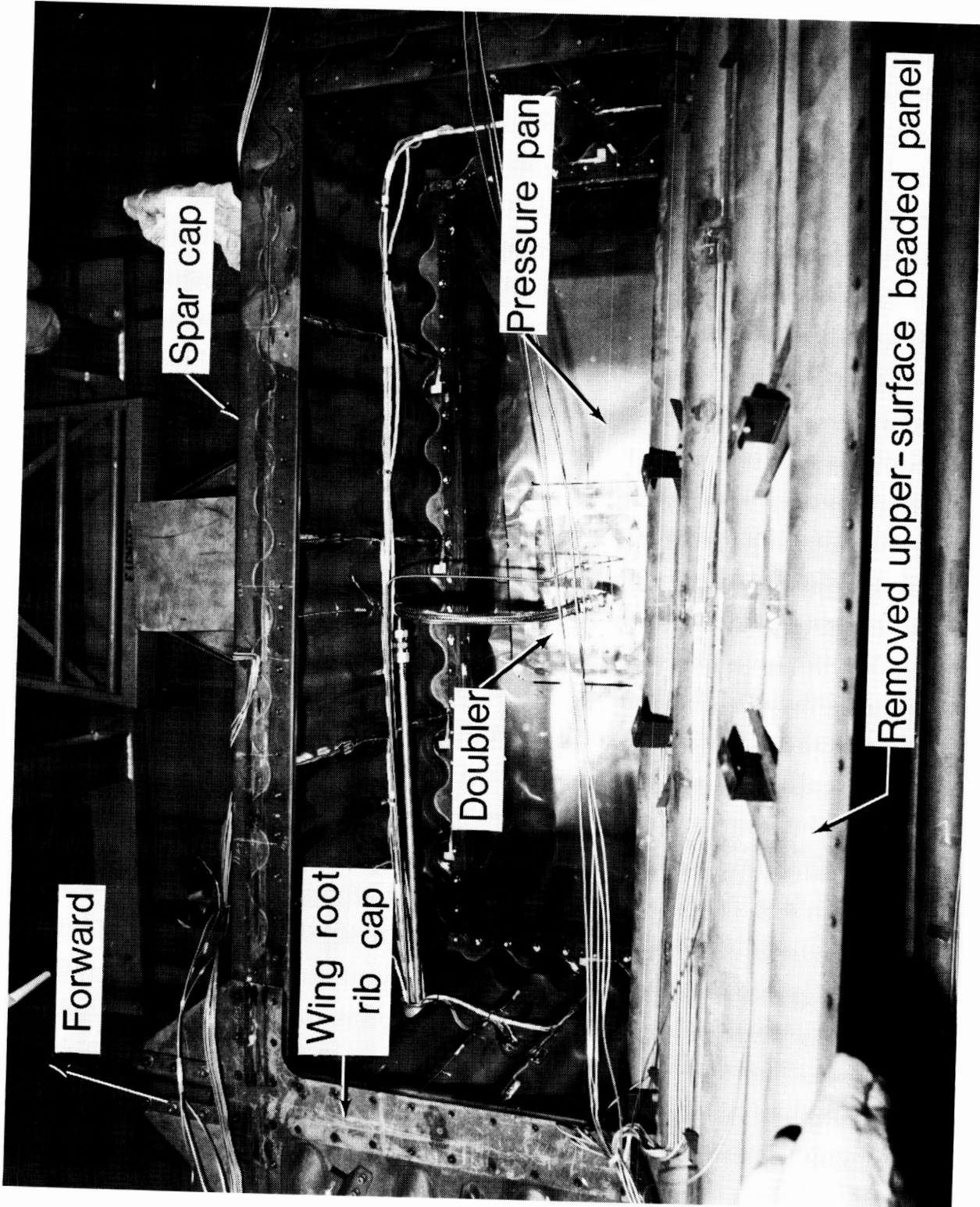
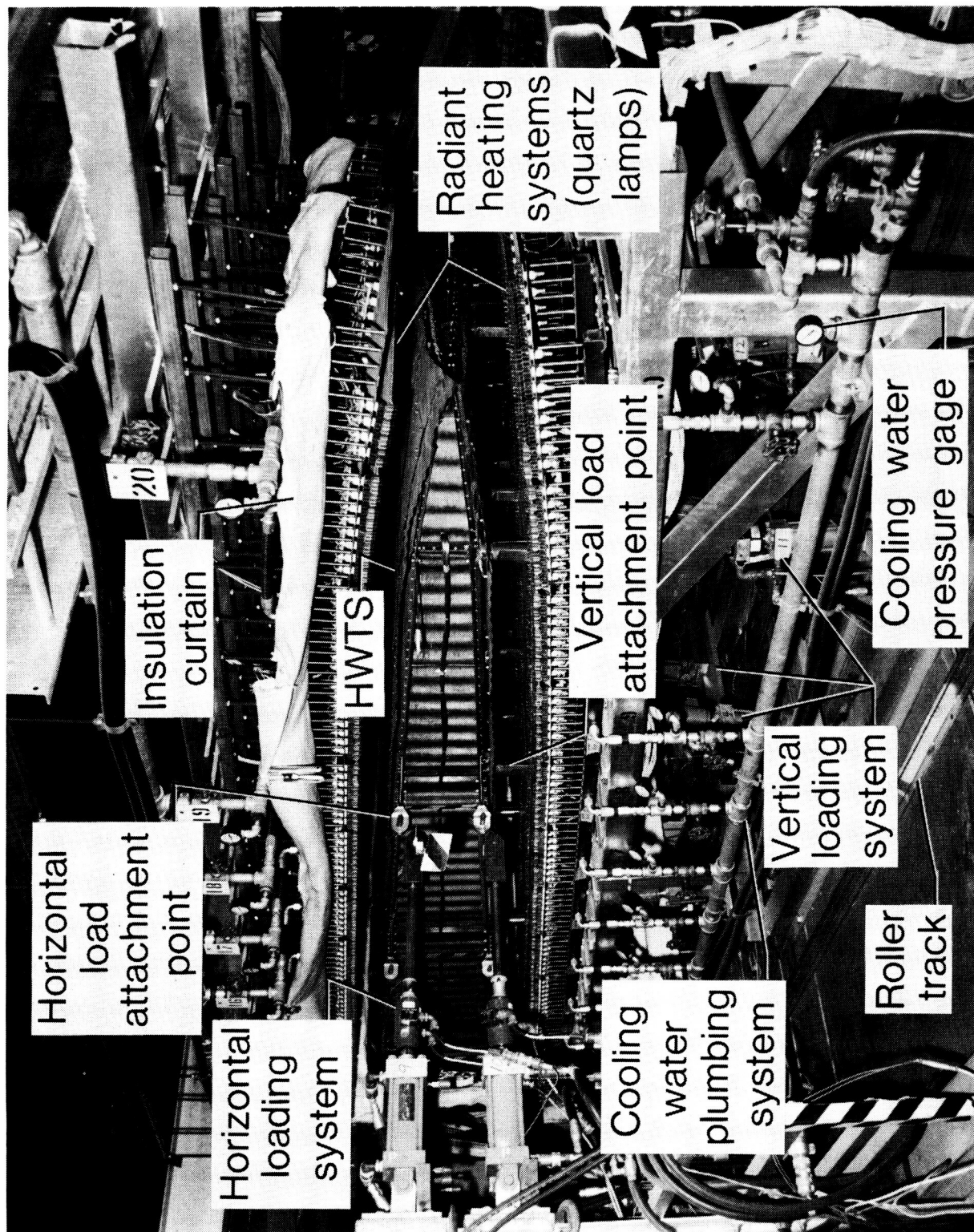


Figure 11. Applied load distribution on HWTS and locations of five test tubular panels.



L-86-352

Figure 12. Interior of HWTs wing root bay showing pressure pan.



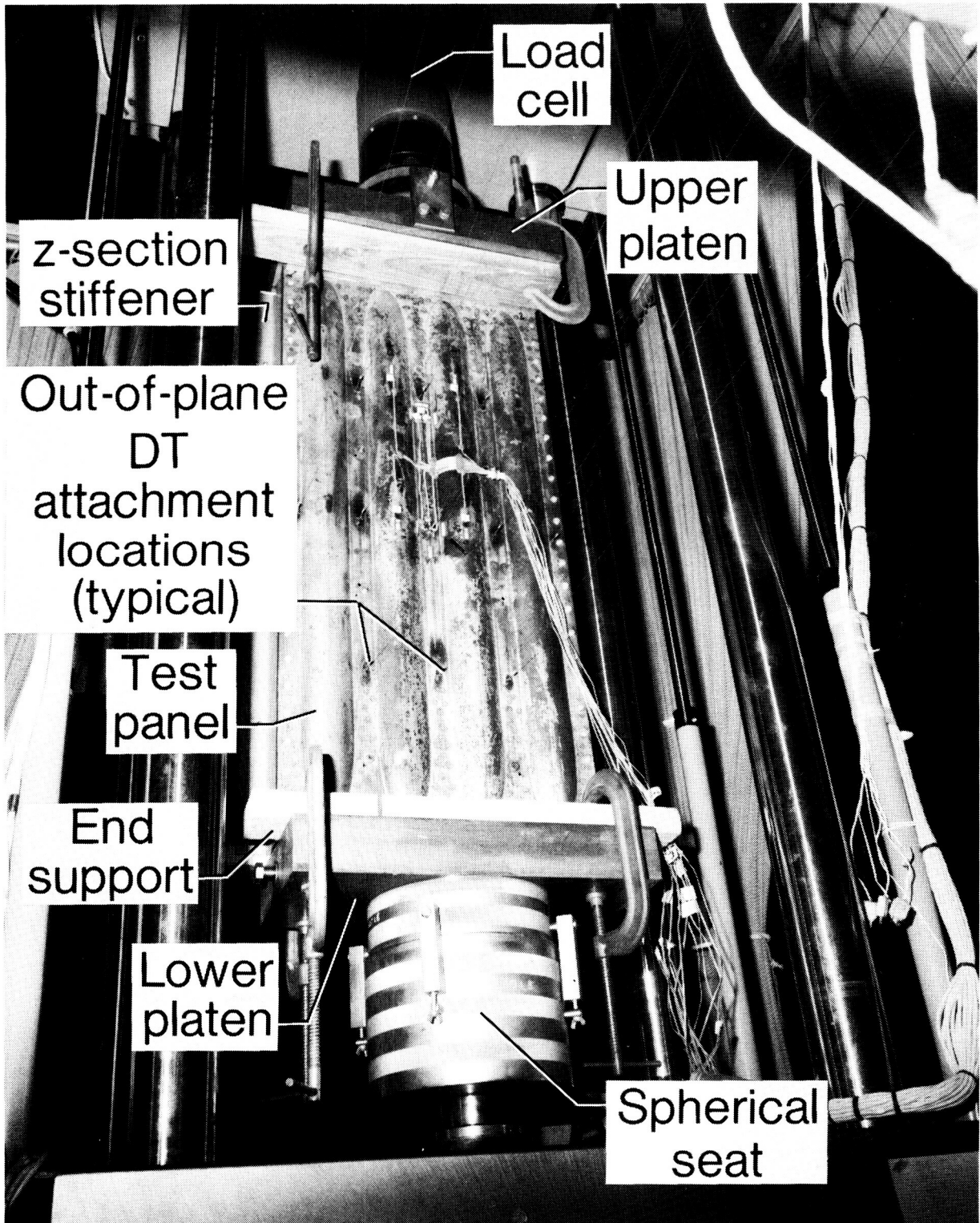
L-86-353

Figure 13. Hypersonic wing test structure combined mechanical and thermal loading test setup.



L-86-354

Figure 14. Radiant heating system for HWT/S.



L-86-355

Figure 15. Tubular panel installed in testing machine for axial compression buckling test.

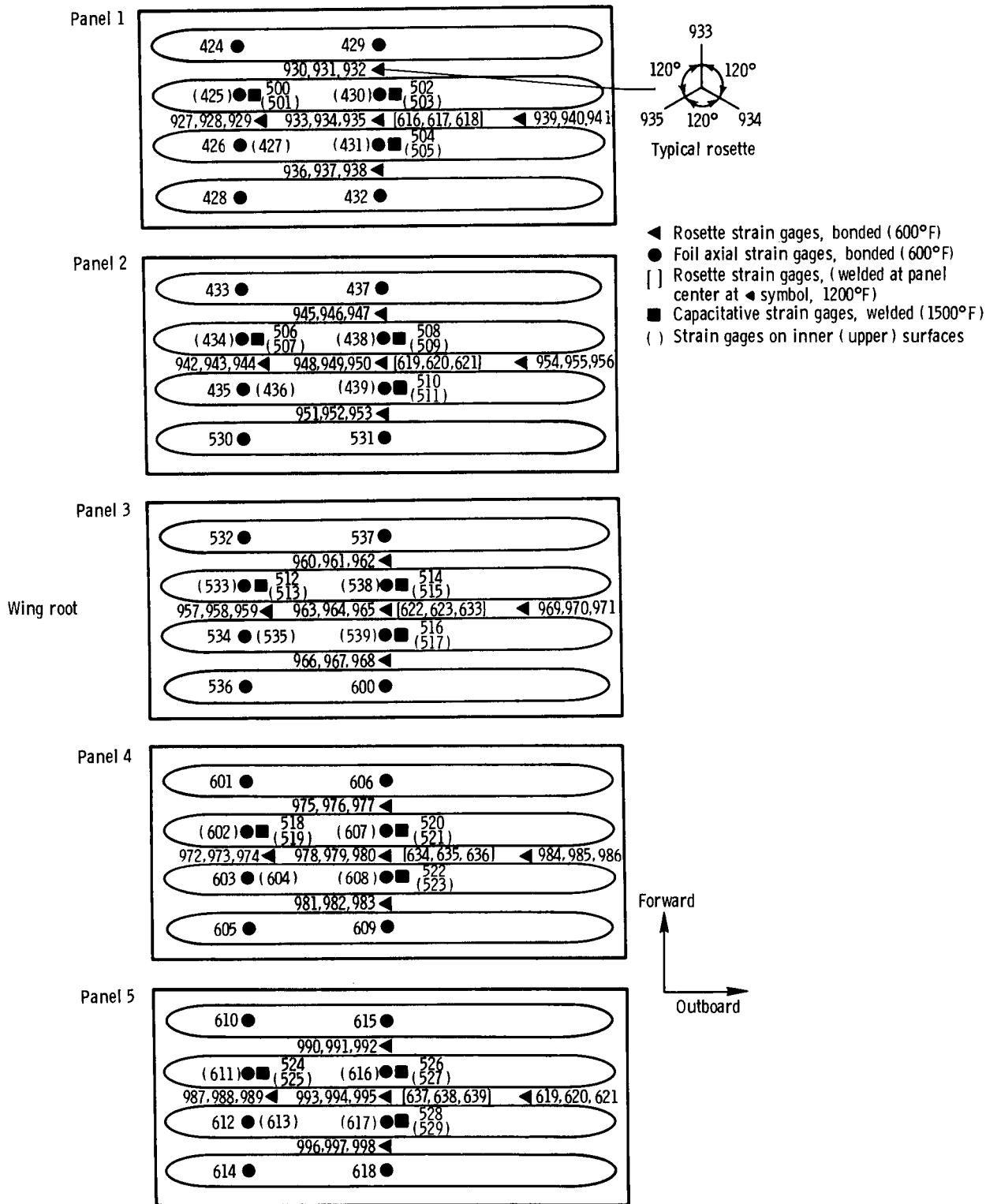
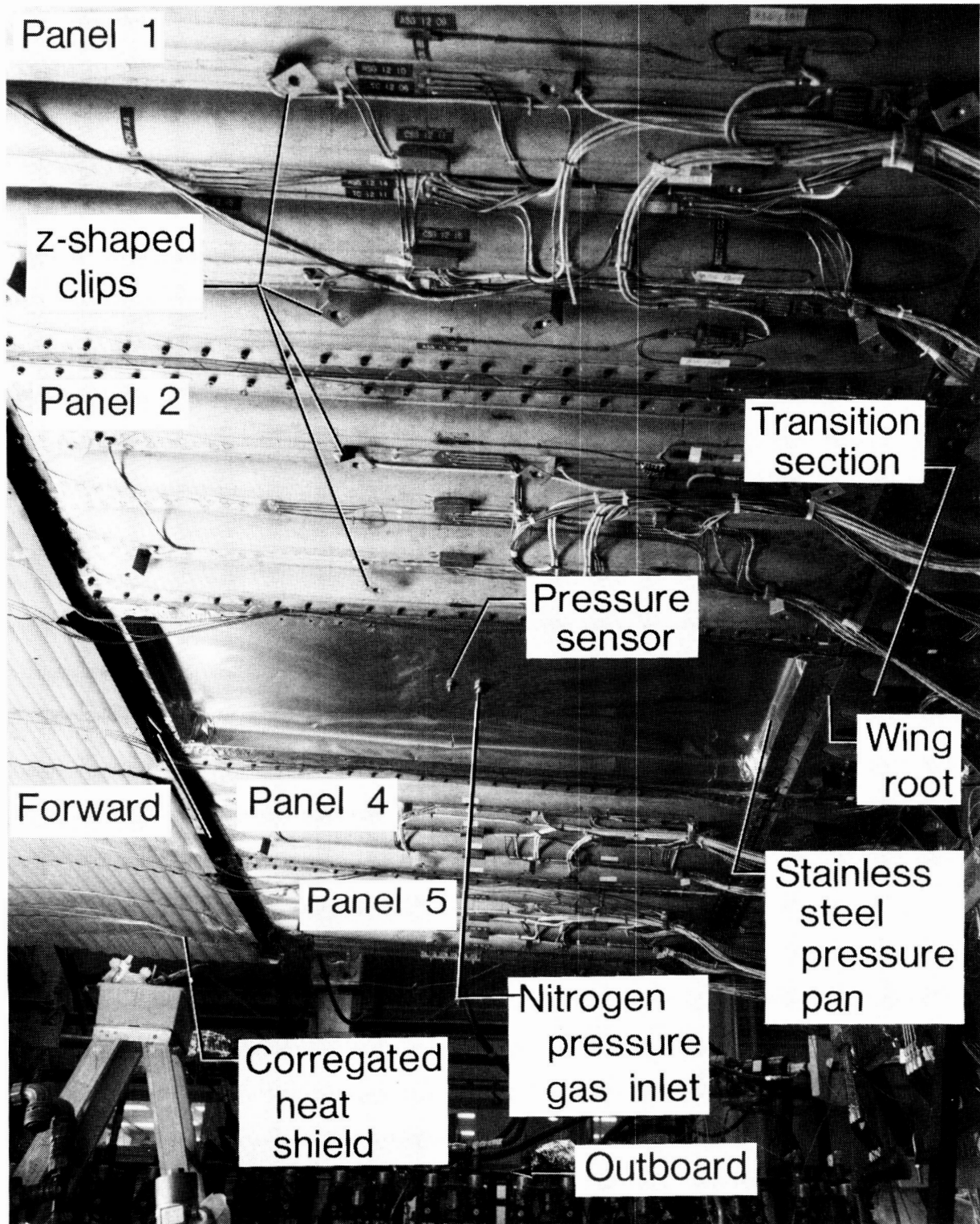


Figure 16. Locations of strain gages on five tubular test panels. View looking downward.



L-86-356
Figure 17. Strain gage and thermocouple (TC) instrumentation on outer (lower) surface of test panel 5.



L-86-357

Figure 18. Four René 41 tubular panels attached to hypersonic wing test structure for buckling tests. View looking up and aft at the lower side of test structure. Panel 3 removed to show pressure pan interior.

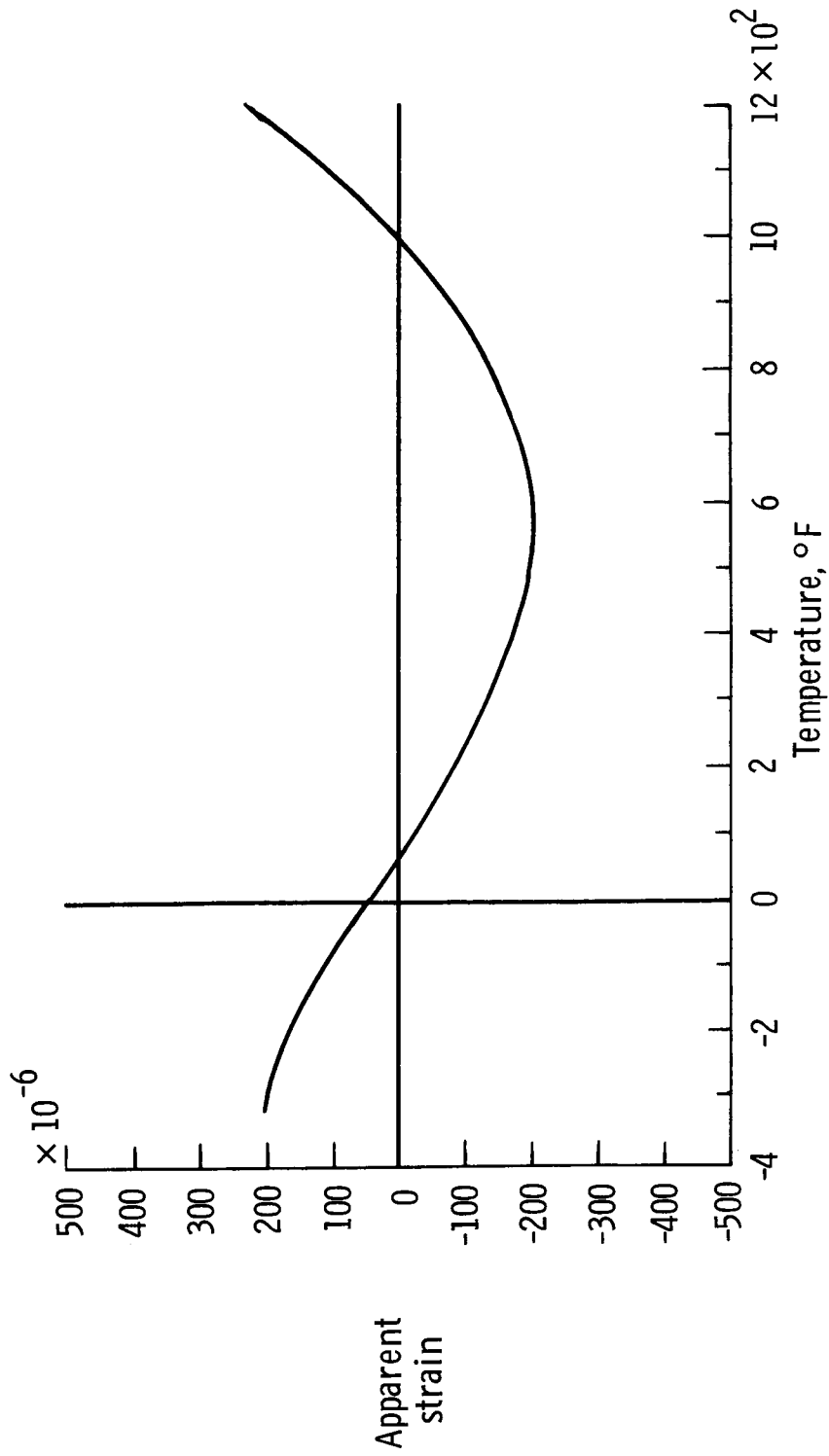
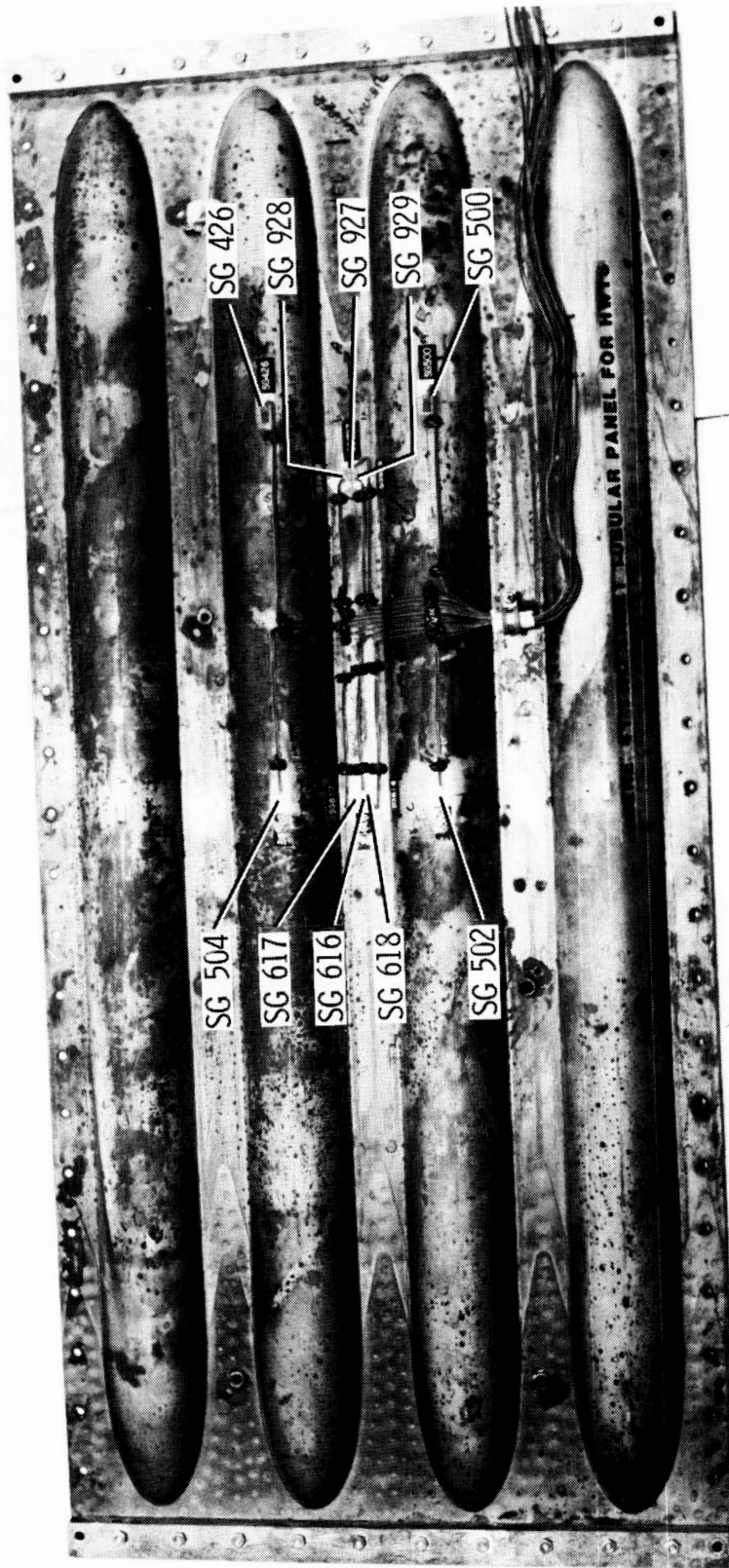
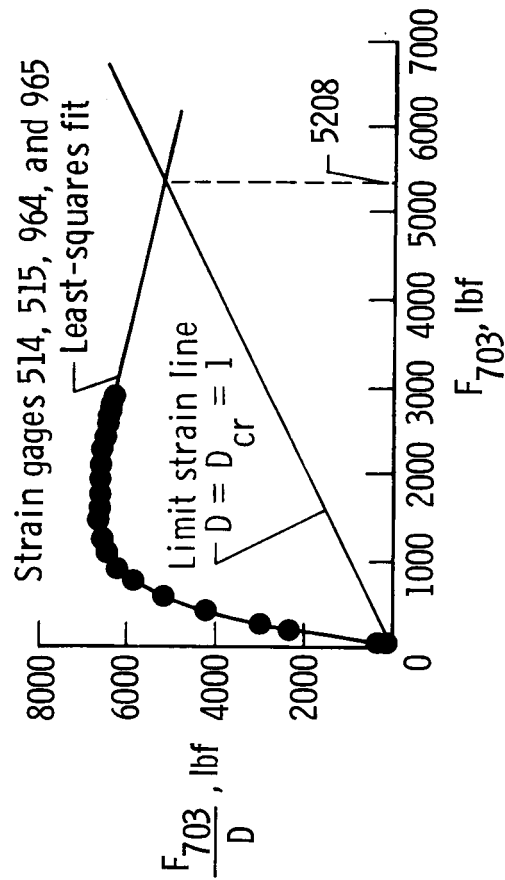


Figure 19. Apparent strain as function of temperature for weldable strain gages mounted on René 41 tubular panels.

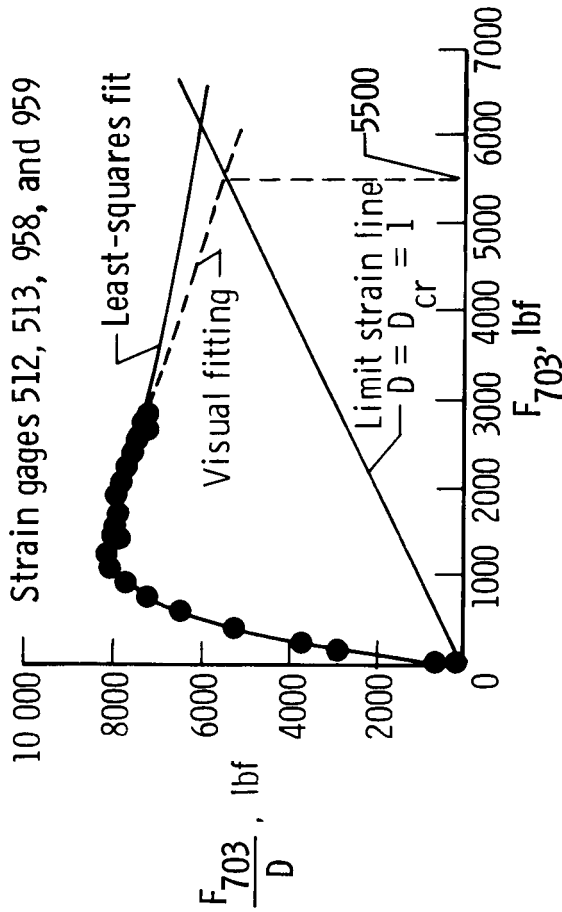


L-86-358

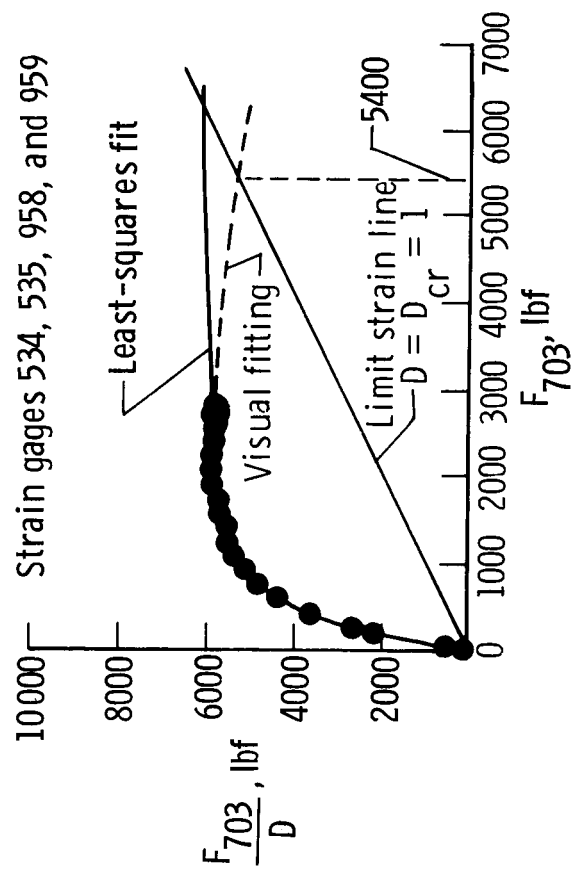
Figure 20. Strain gage instrumentation on outer surface of test panel I for room-temperature, pure-compression, single-panel buckling test.



(a) $\frac{N_{xy}}{N_x} = 0.56$.

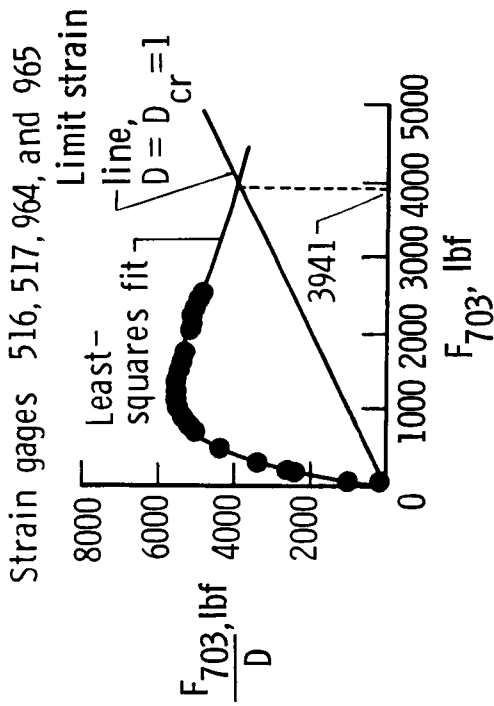


(b) $\frac{N_{xy}}{N_x} = 0.49$.

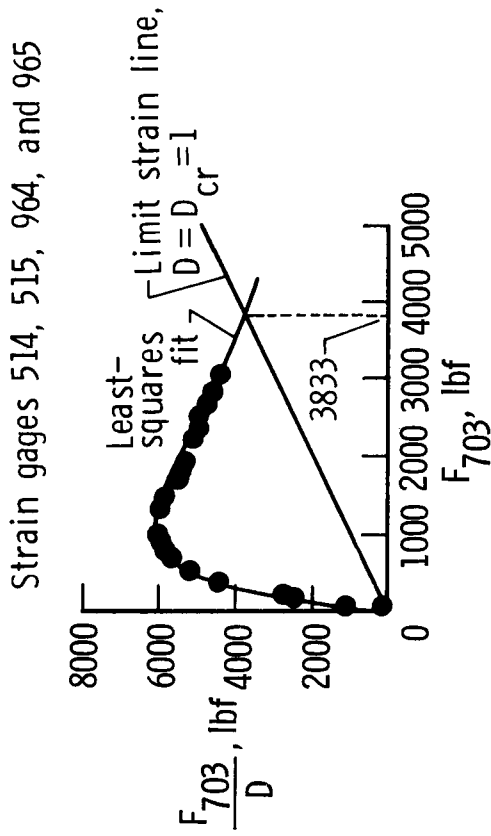


(c) $\frac{N_{xy}}{N_x} = 0.49$.

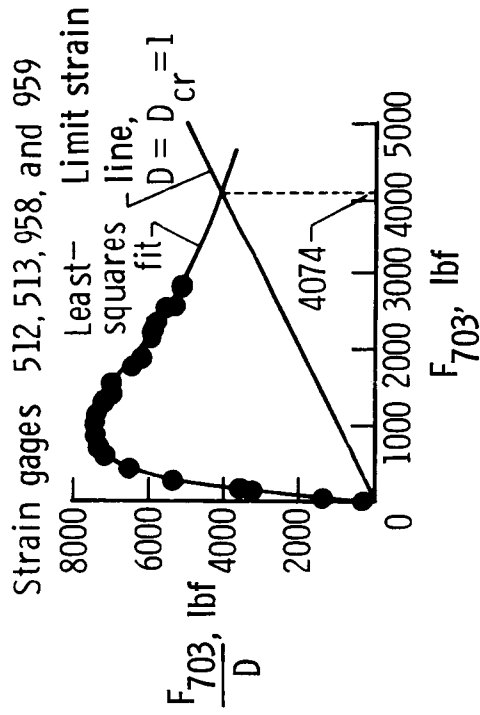
Figure 21. Force/stiffness plots for panel 3 test 4.2.6. $T = 70^\circ\text{F}$; $p = 0.75$ psi.



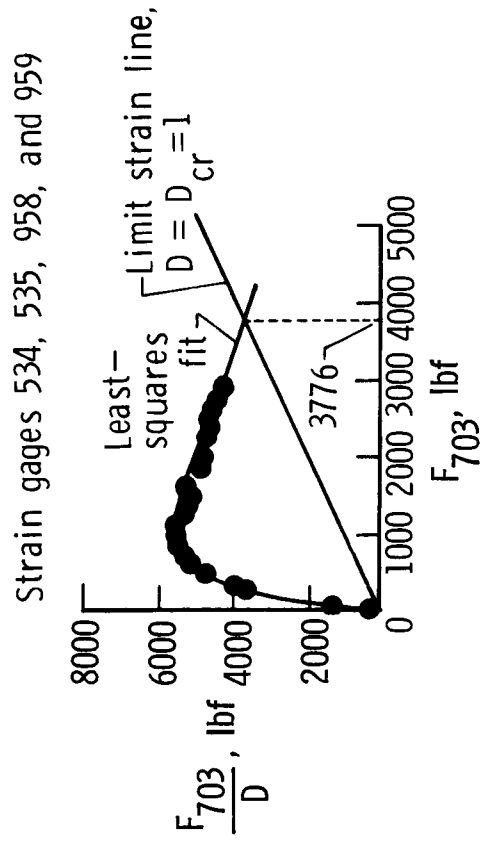
(a) $\frac{N_{xy}}{N_x} = 3.22.$



(b) $\frac{N_{xy}}{N_x} = 3.22.$

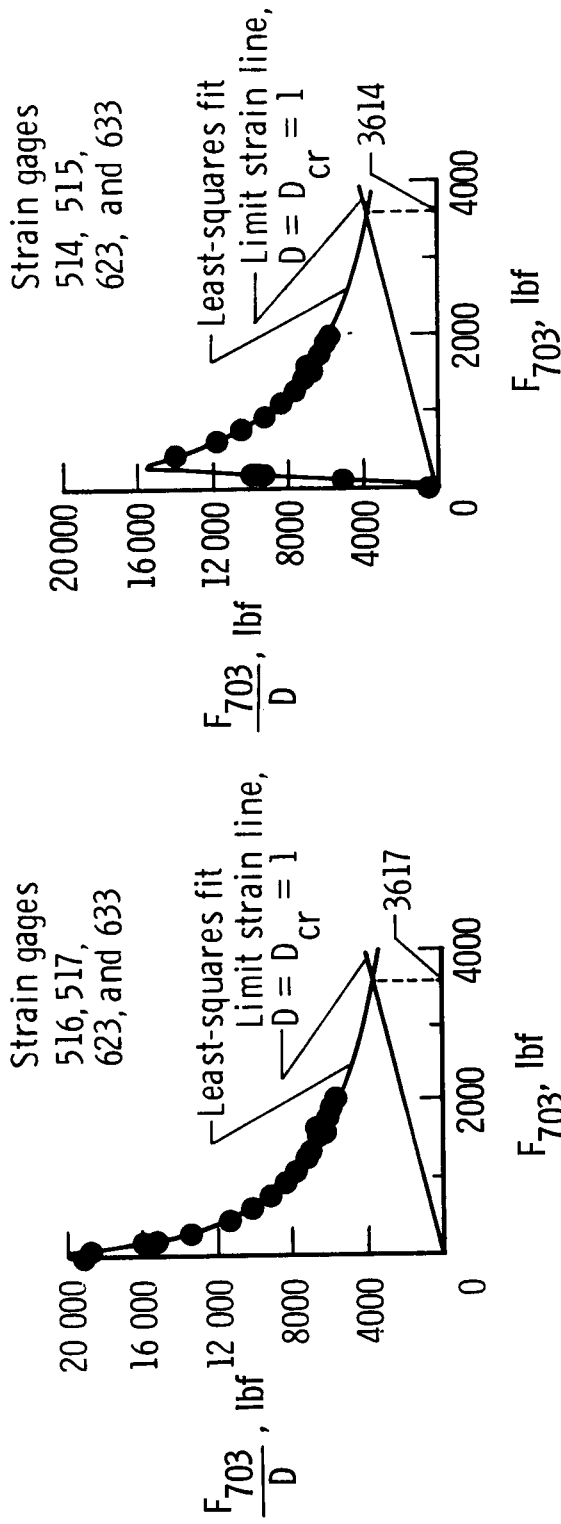


(c) $\frac{N_{xy}}{N_x} = 3.19.$



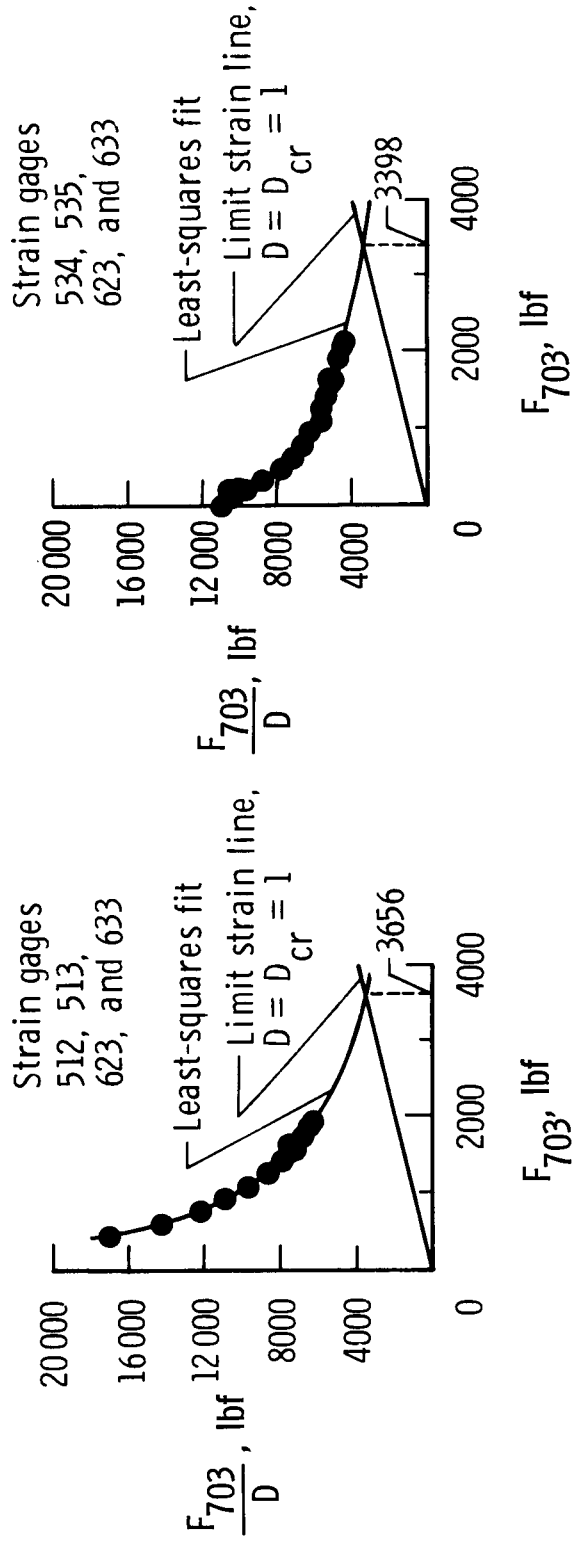
(d) $\frac{N_{xy}}{N_x} = 3.19.$

Figure 22. Force/stiffness plots for panel 3 test 4.4.6. $T = 70^\circ\text{F}$; $p = 0.75$ psi.

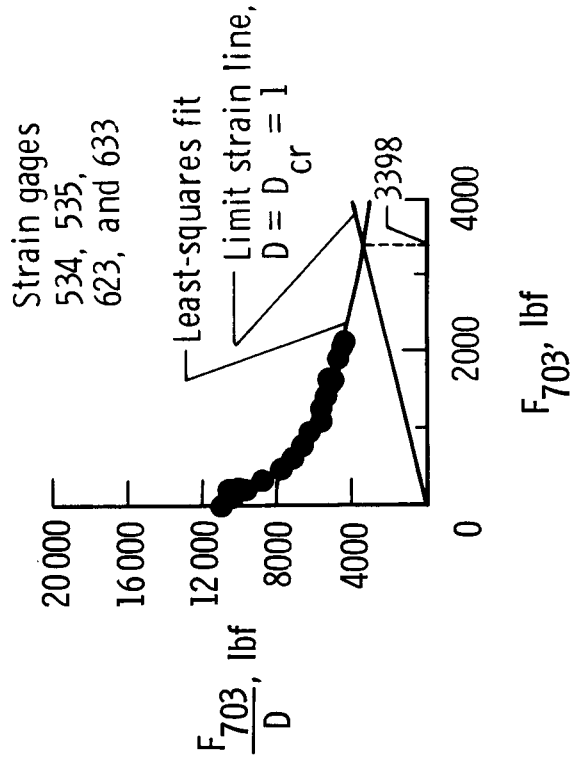


(a) $\frac{N_{xy}}{N_x} = 1.22$.

(b) $\frac{N_{xy}}{N_x} = 1.22$.

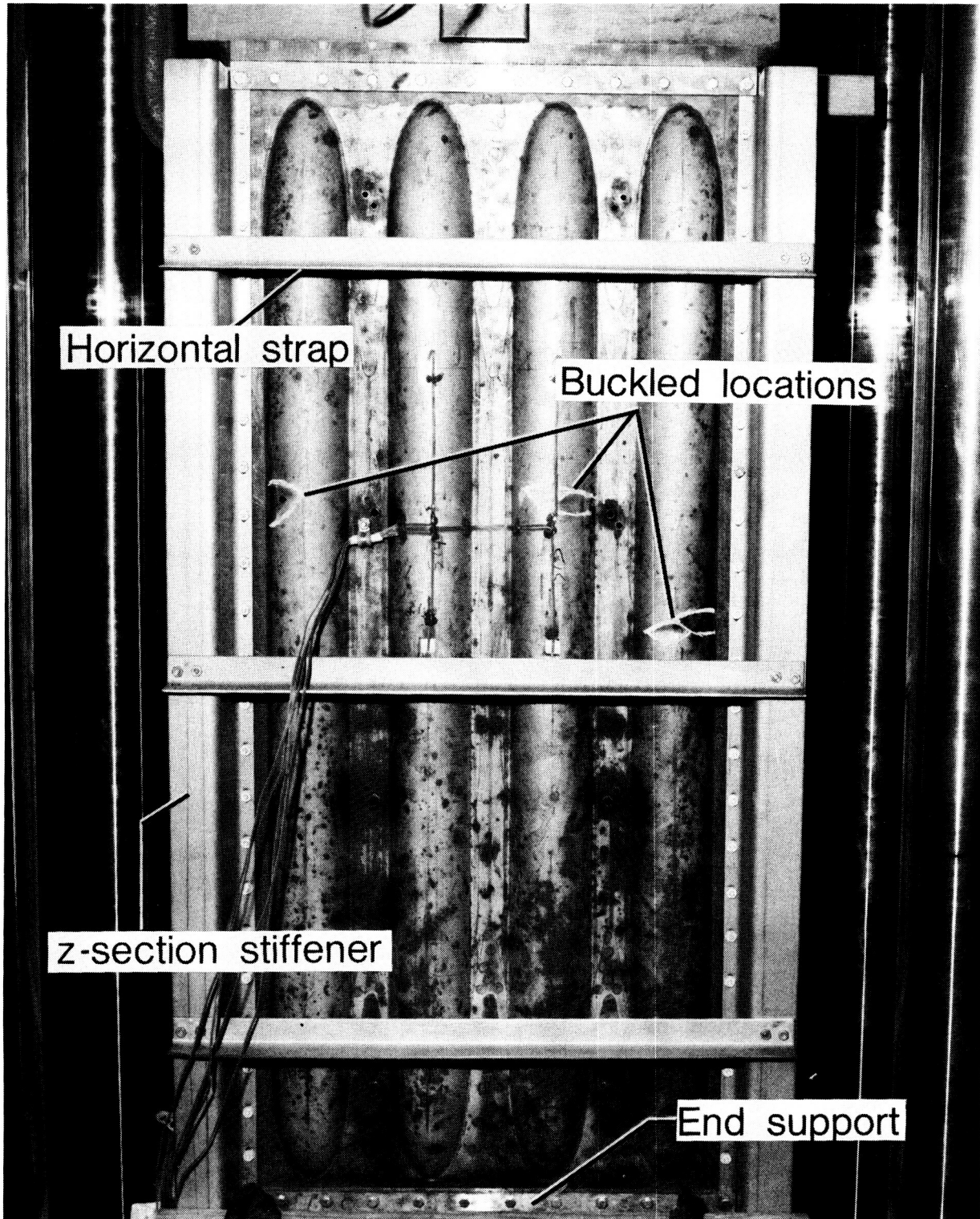


(c) $\frac{N_{xy}}{N_x} = 1.22$.



(d) $\frac{N_{xy}}{N_x} = 1.22$.

Figure 23. Force/stiffness plots for panel 3 test 4.3.4. $T = 70^\circ\text{F}$; $p = 0$ psi.



L-86-359

Figure 24. Buckled panel 3 after compression buckling test.

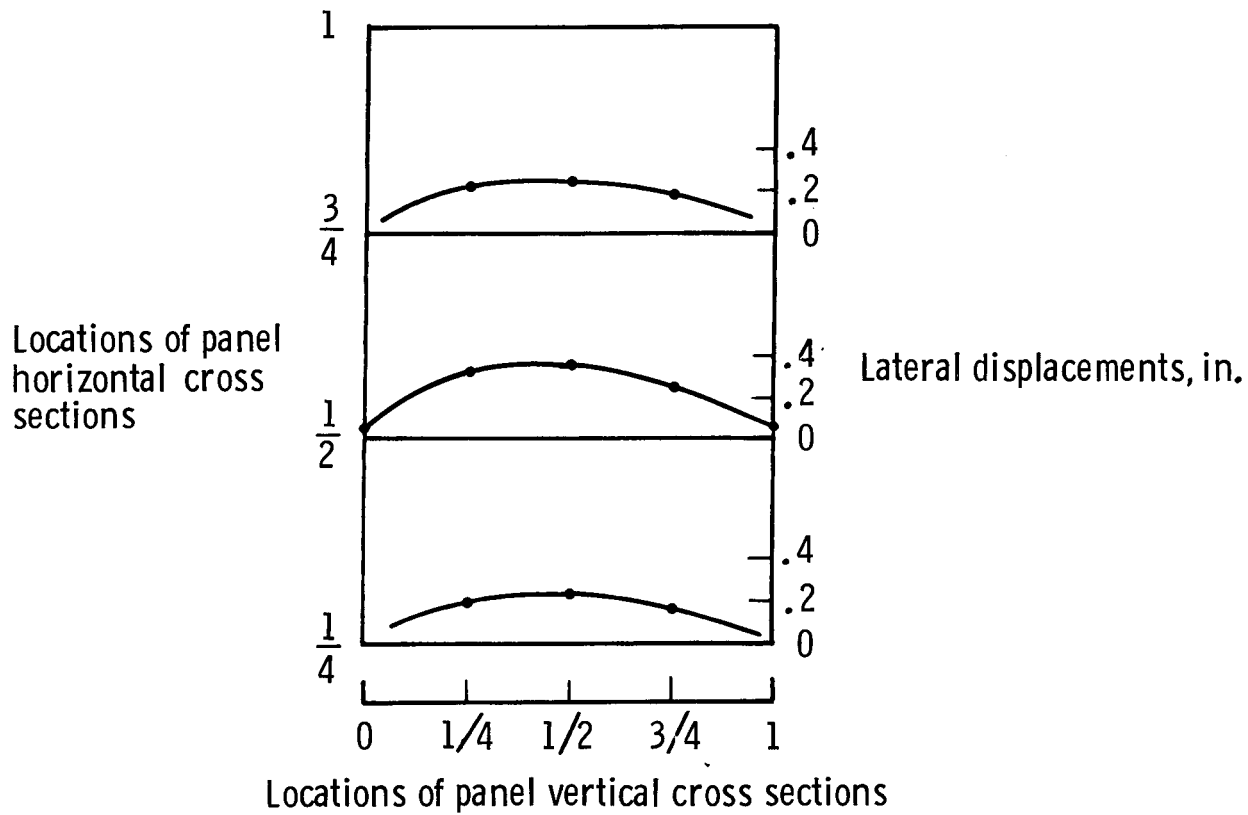
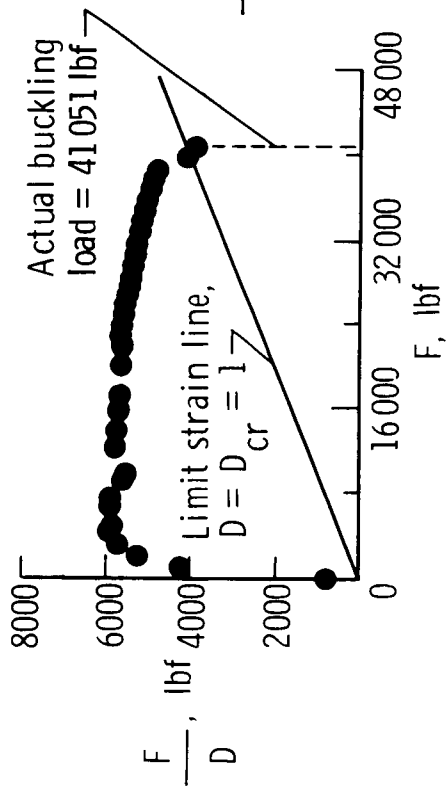
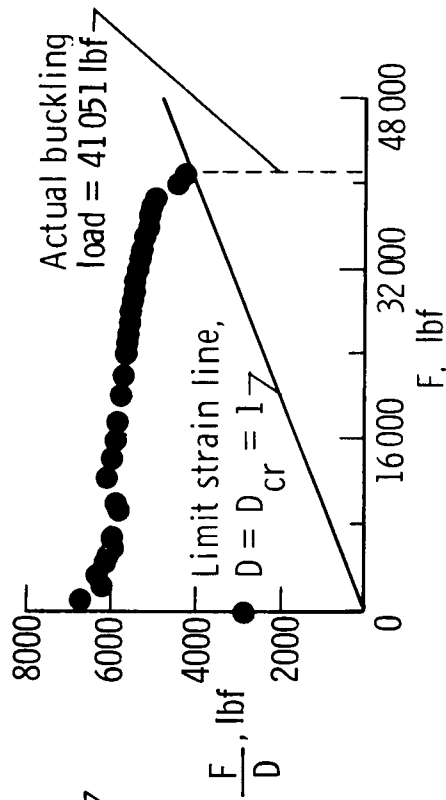


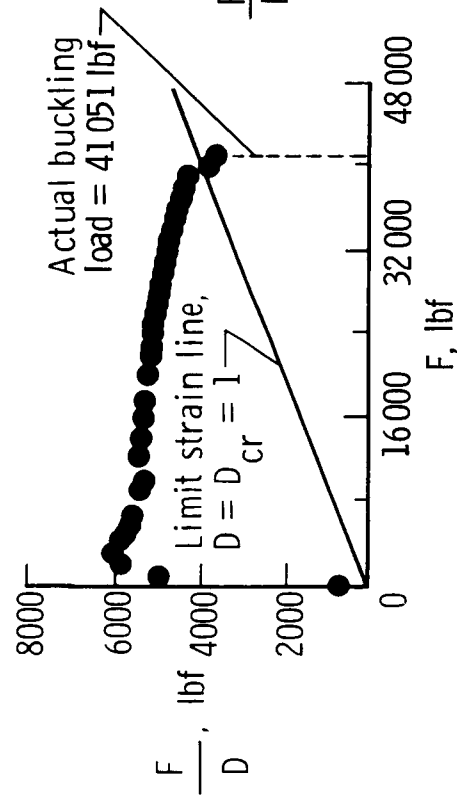
Figure 25. Out-of-plane displacements of test panel 3 immediately before buckling for single-panel compression test.



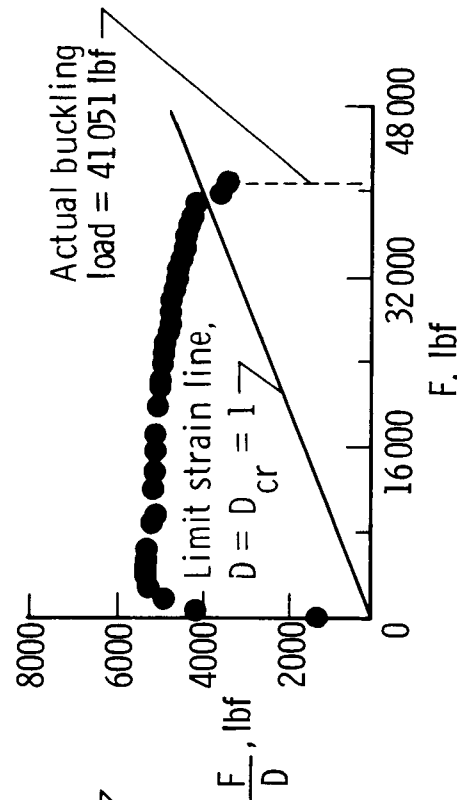
(a) Strain gages SG 516, SG 517, RSG 623, and RSG 633.



(b) Strain gages SG 514, SG 515, RSG 623, and RSG 633.

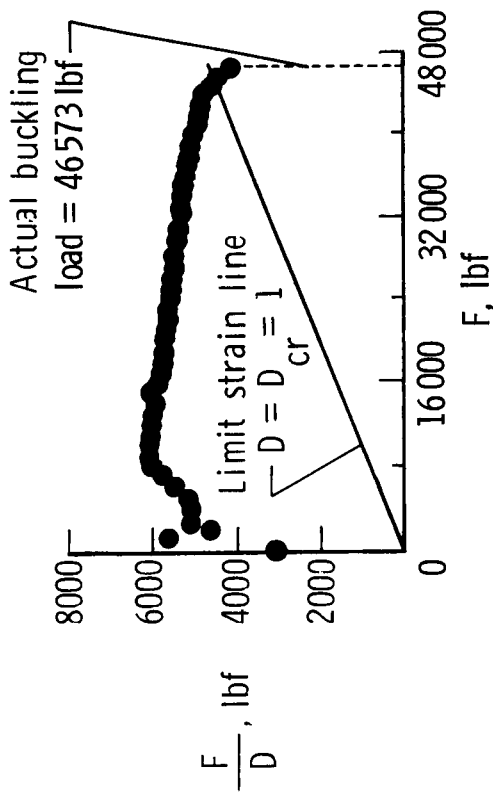


(c) Strain gages SG 512, SG 513, RSG 958, and RSG 959.

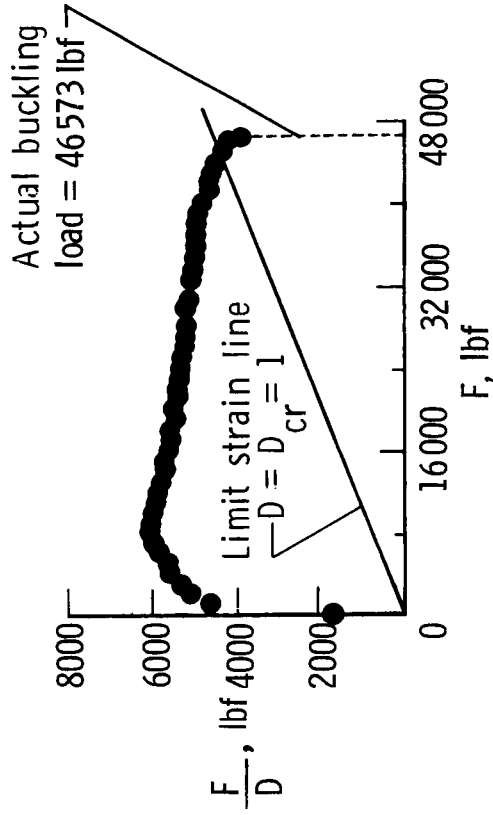


(d) Strain gages SG 534, SG 535, RSG 958, and RSG 959.

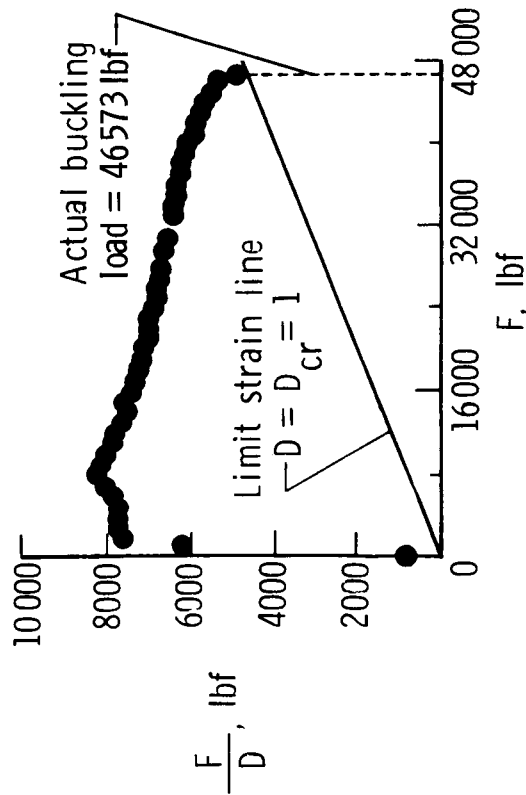
Figure 26. Force/stiffness plots for single-panel compression test to failure for panel 3. $T = 70^{\circ}\text{F}$; $p = 0$ psi.



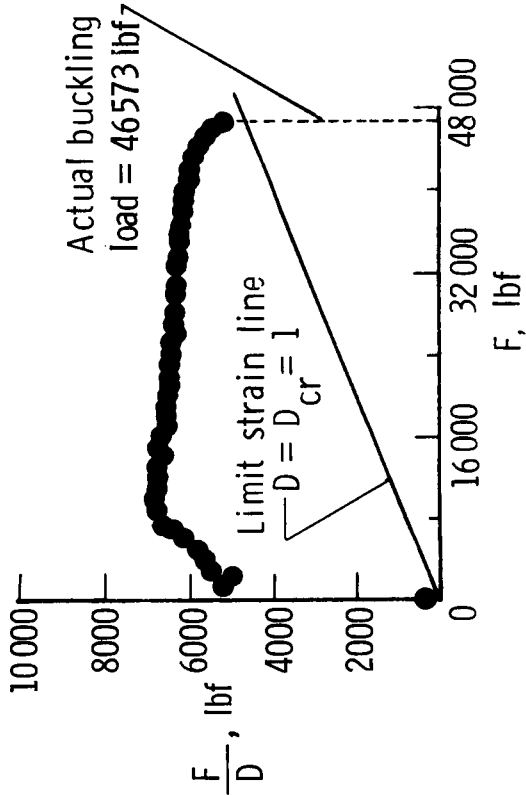
(a) Strain gages SG 504, SG 505, RSG 617, and RSG 618.



(b) Strain gages SG 502, SG 503, RSG 617, and RSG 618.

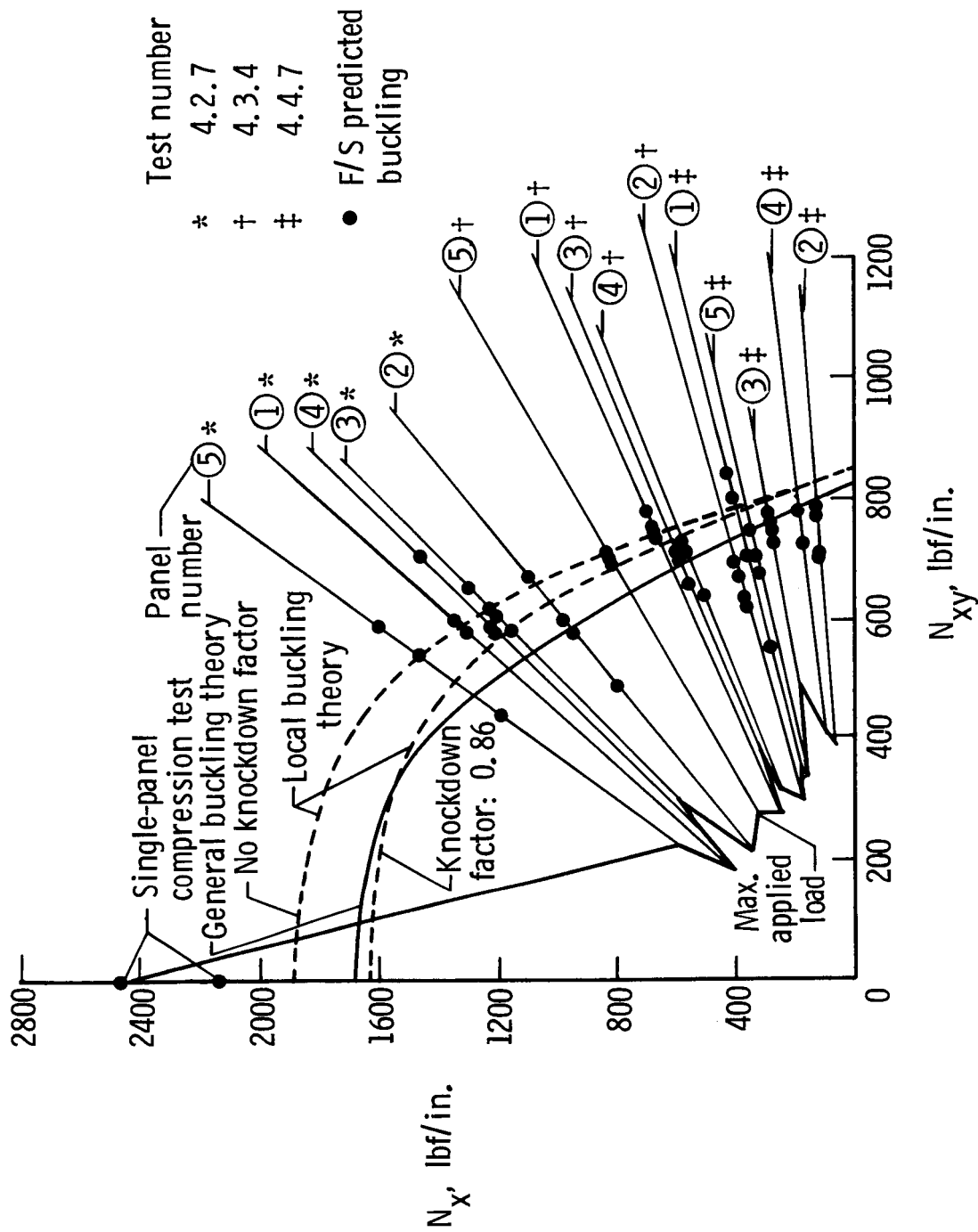


(c) Strain gages SG 500, SG 501, RSG 928, and RSG 929.



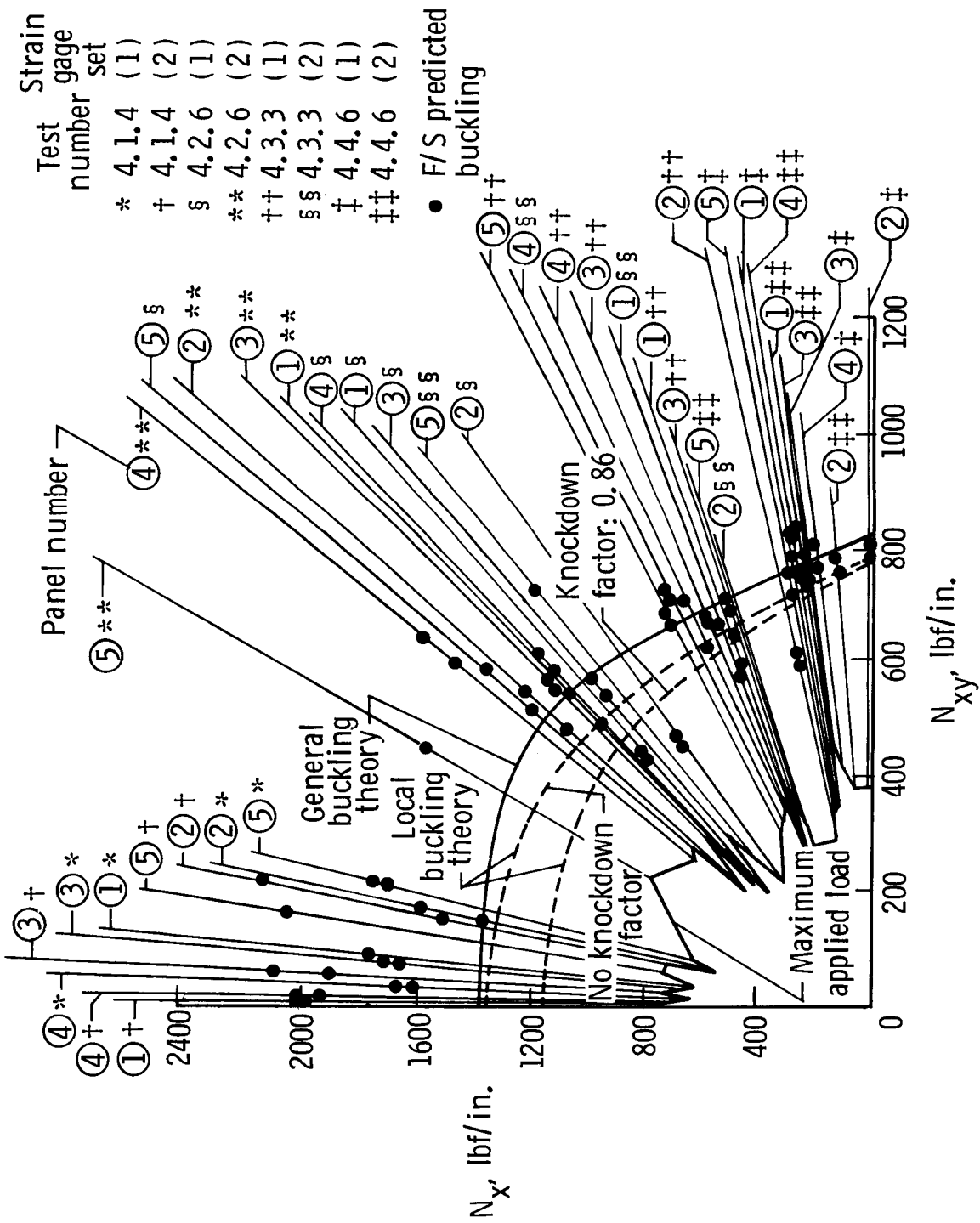
(d) Strain gages SG 426, SG 427, RSG 928, and RSG 929.

Figure 27. Force/stiffness plots for single-panel compression test to failure for panel 1. $T = 70^{\circ}\text{F}$; $p = 0$ psi.



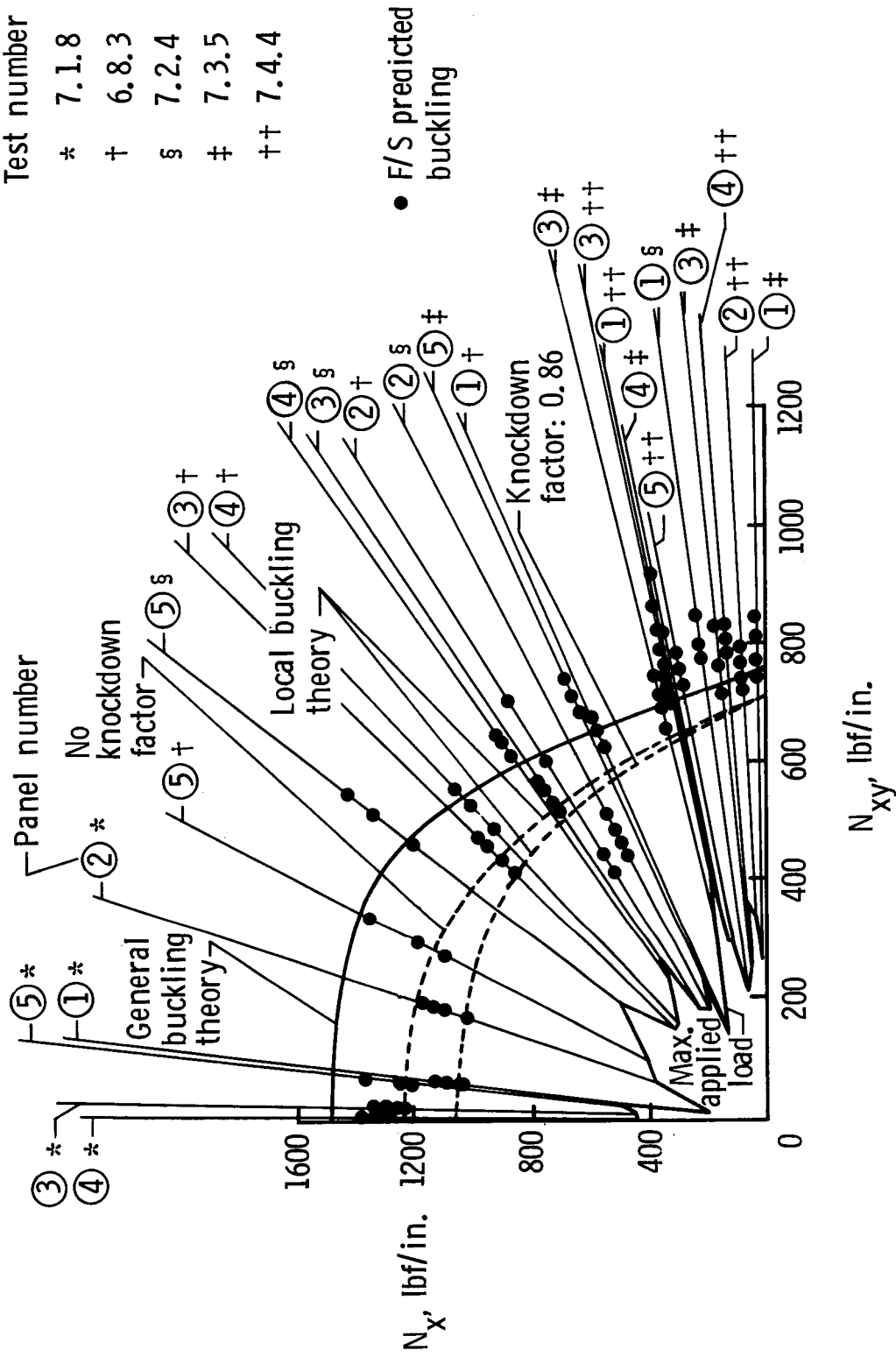
(a) $T = 70^{\circ}\text{F}$; $p = 0$ psi.

Figure 28. Buckling interaction plots for five René 41 tubular panels.



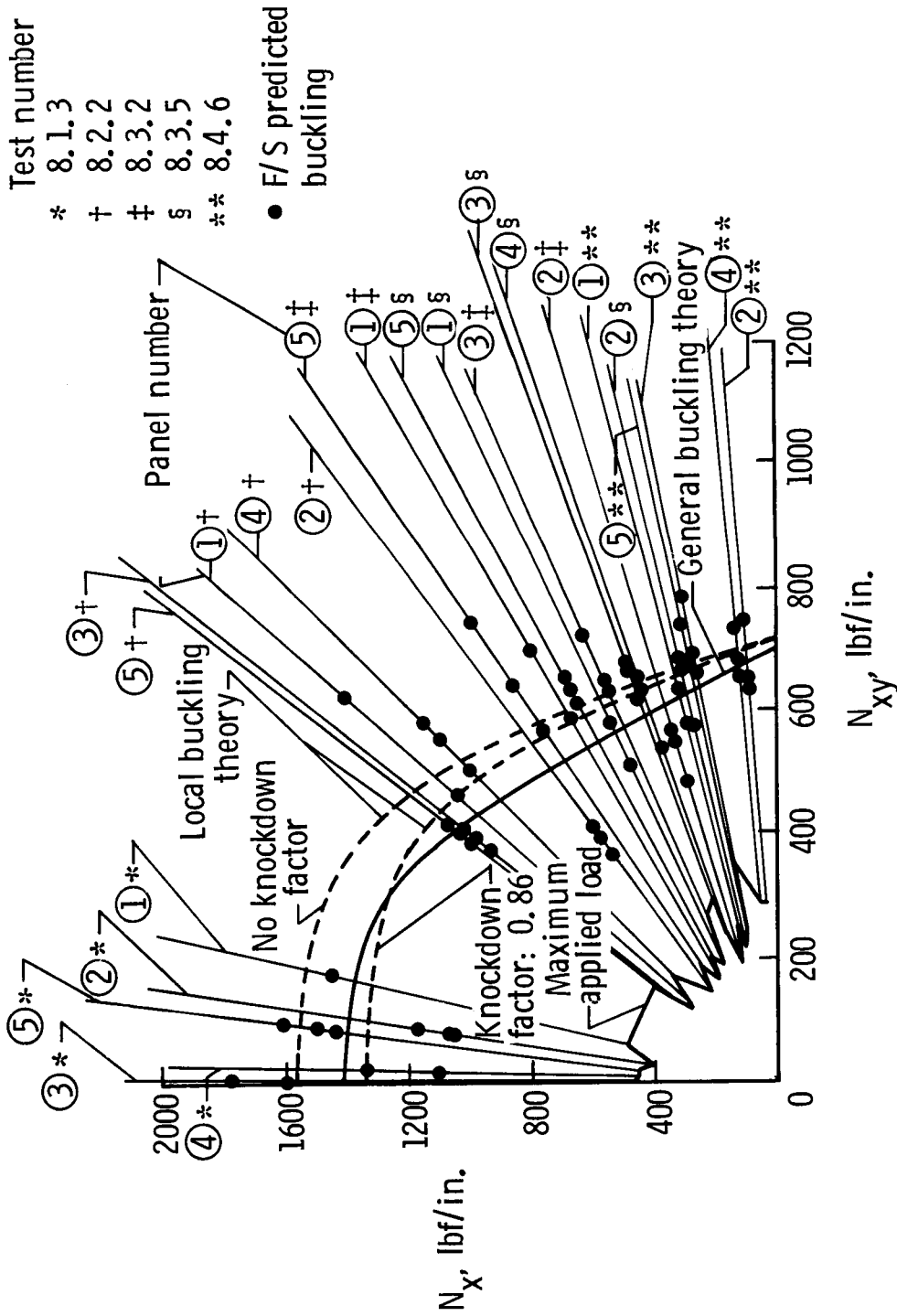
(b) $T = 70^{\circ}F$; $p = 0.75$ psi. Strain gage set refers to locations 1 and 2 of table 4. Figure 28. Continued.

Test number
* 7.1.8
+ 6.8.3
§ 7.2.4
7.3.5
++ 7.4.4



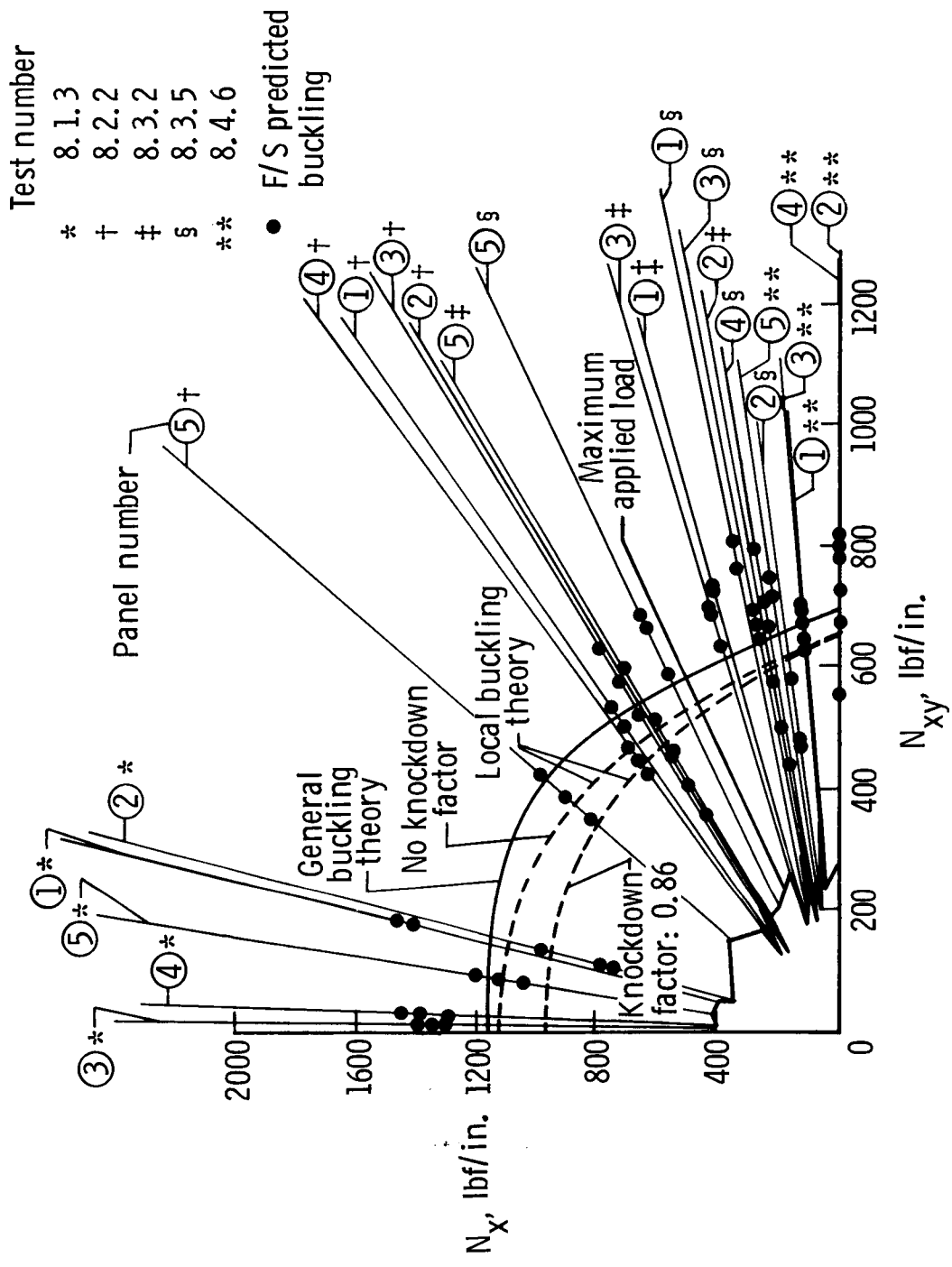
(c) $T = 550^{\circ}\text{F}$; $p = 0.75$ psi.

Figure 28. Continued.



(d) $T = 1000^{\circ}\text{F}$; $p = 0$ psi.

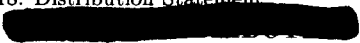
Figure 28. Continued.



(e) $T = 1000^\circ\text{F}$; $p = 0.75$ psi.

Figure 28. Concluded.

Standard Bibliographic Page

1. Report No. NASA TM-87756	2. Government Accession No.	3. Recipient's Catalog No.	
4. Title and Subtitle Buckling Characteristics of Hypersonic Aircraft Wing Tubular Panels		5. Report Date December 1986	
		6. Performing Organization Code 506-43-31-04	
7. Author(s) William L. Ko, John L. Shideler, and Roger A. Fields		8. Performing Organization Report No. L-16128	
		10. Work Unit No.	
9. Performing Organization Name and Address NASA Langley Research Center Hampton, VA 23665-5225		11. Contract or Grant No.	
		13. Type of Report and Period Covered Technical Memorandum	
12. Sponsoring Agency Name and Address National Aeronautics and Space Administration Washington, DC 20546-0001		14. Sponsoring Agency Code	
		15. Supplementary Notes William L. Ko: Ames-Dryden Flight Research Facility, Edwards, California. John L. Shideler: Langley Research Center, Hampton, Virginia. Roger A. Fields: Ames-Dryden Flight Research Facility, Edwards, California.	
16. Abstract The buckling characteristics of René 41 tubular panels installed as wing panels on a hypersonic wing test structure (HWTS) were determined nondestructively through use of a force/stiffness technique. The nondestructive buckling tests were carried out under different combined load conditions and different temperature environments. Two panels were subsequently tested to buckling failure in a universal tension-compression testing machine. In spite of some data scattering because of large extrapolations of data points resulting from termination of the test at a somewhat low applied load, the overall test data correlated fairly well with theoretically predicted buckling interaction curves. The structural efficiency of the tubular panels was slightly higher than that of the beaded panels which they replaced.			
17. Key Words (Suggested by Authors(s)) Hypersonic wing test structure Tubular panels Nondestructive test Buckling		18. Distribution Statement  UNTIL DECEMBER 1988 Subject Category 39	
19. Security Classif.(of this report) Unclassified	20. Security Classif.(of this page) Unclassified	21. No. of Pages 68	22. Price c